Title
The Search For Hidden Mixing; Analysis of the Collective and Intrusive Instabilities for Low Prandtl Number and Diffusivity Ratio Systems

Author
Medrano, Michael

Publication Date
2014

UNIVERSITY OF CALIFORNIA

SANTA CRUZ

THE SEARCH FOR HIDDEN MIXING; ANALYSIS OF THE COLLECTIVE AND INTRUSIVE INSTABILITIES FOR LOW PRANDTL NUMBER AND DIFFUSIVITY RATIO SYSTEMS

A thesis submitted in partial satisfaction
of the requirements for the degree of

MASTER OF SCIENCE

in

PHYSICS

by

Michael Medrano

June 2014

The thesis of Michael Medrano
is approved:

____
Professor Pascale Garaud, Chair

____
Professor Stefano Profumo

____
Professor Michael Dine

____
Tyrus Milller
Vice Provost and Dean of Graduate Studies

Contents

List of Figures **v**

List of Tables **viii**

Abstract **ix**

Acknowledgements **x**

1 Introduction: **1**

1.1 Motivation: 1

1.2 Small- Scale Double- Diffusive Instabilities: 4

1.3 Mathematical Model of Fingering Instabilities 6

2 Large Scale Double Diffusive Instabilities **15**

2.1 The collective and intrusive instabilities 15

2.2 Unified Mathematical Model for Double Diffusive Instabilities 17

3 Results: **26**

3.1 The Laminar Case: Oscillatory and Intrusive modes at $\phi = 10^{-3}$ 26

3.1.1 Intrusions 26

3.1.2 Oscillatory Modes 31

3.2 The Turbulent Case: The Collective Instability at $\phi = 0$ 34

3.3 The Turbulent Case: Oscillatory and Intrusive Modes at $\phi = 10^{-3}$ 37

3.3.1 Direct Modes: 37

3.3.2 Oscillatory Modes 39

4 Conclusion **42**

Appendices **46**

A The Method of Dominant Balances: Intrusions **46**

B Rough Approximation for Intrusive Modes **50**

C The Method of Dominant Balances: Oscillatory Modes **53**

D Rough Approximation for Oscillatory Modes **55**

References **58**

List of Figures

1 The internal structure of a low mass RGB star. Shortly after the end of the Main Sequence ($\approx$ 10 Gyr), the convective region is restricted to $m/M_{\odot} \approx 1$. The hydrogen burning shells are located much deep in the star, $m/M_{\odot} \approx .2$. The "first dredge up" occurs at $t \approx 12.3$ Gyr. The luminosity bump occurs shortly after- marked by the green curve L_H. Courtesy K. Moore. 2

2 Mean Molecular Weight μ as a function of reduced mass coordinate $m/M_{\odot}$ after HBS moves past lowest point of the first dredge up. We see an inverse μ gradient since $^3(^3\mathrm{He},2\mathrm{p})^4$ is the energetically preferred reaction in the cooler region of the HBS- the HBS region closest to the surface of the star. Courtesy Garaud. 3

3 The ODDC Instability. The water parcel (black circle) is perturbed downward. The dotted black line shows the motion of the parcel in the case temperature diffusion is negligible and hence, the density of the parcel is constant. Notice, that in this case, the trajectory is purely oscillatory. The black line shows the case where temperature diffusion occurs much more rapidly than diffusion due to salinity. The result of this process is to amplify amplitude of the wave motion in the vertical. From Garaud (2013) 5

4 The Basic Fingering Instability. Here a relatively warm and salty water parcel (black circle) is perturbed downward. Since, temperature diffusion occurs very rapidly, the parcel becomes much cooler and hence, denser than neighboring parcel and begins to sink. From Garaud (2013) 6

5 A comparison of the numerical and asymptotic values of the growth rate λ as a function of r. 12

6 A comparison of the Nu_0 corresponding to fingering convection with Nu_0 required by observations in order to explain the missing mixing problem along the RGB. Courtesy Garaud. 14

7 The Intrusive Instability. The dotted lines correspond to the mean isohalines. Although the isotherms are not shown, there slope very close follows the isohalines. From Radko (2013) . 16

8 Flower Plots obtained by solving Equation (51) for λ for $Pr = 7$, $\tau = .01$ at (a) $R_0 = 7$, (b) $R_0 = 4.0$, (c) $R_0 = 1.5$. $\phi = 0/.01$ in the left/right columns. This figure recovers Figure 4 of Traxler et al. (2011). 24

9 Flower Plots for $Pr = \tau = 10^{-6}$ and $\phi = 10^{-3}$ at various R_0 ($A_1 = A_2 = 0$ and $Nu_0 = 1$). An effect of increasing R_0 is that the intrusive mode is only supported for negative k. 27

10 λ_{max} of direct modes as a function of r. The fingering modes are represented by colored solid lines. These have the distinct feature that $\lambda_{max} \to 0$ as $r \to 1$. λ_{max} for the direct modes with $\phi \neq 0$ are depicted by lines with markers. 28

11 Fingering in the case of lateral intrusions. Here, $T_1 > T_2 > T_3$ and similarly $S_1 > S_2 > S_3$. The dark lines represent isotherms and isohalines. 29

12 l_{max} and k_{max} vs r for the direct modes. We see that for $Pr = \tau \to 10^{-7}$, $l_{max} \to -k_{max}$. . . . 30

13 Flower Plots obtained by solving equation (51) for λ for Pr = τ= 10^{-6} and $\phi = 10^{-3}$. The oscillatory modes are given by the small k "leaf" structures. 32

14 λ_{max} vs r for the oscillatory modes at $\phi = 10^{-3}$ for $Pr = \tau$ varying between 10^{-4} and 10^{-7}. 33

15 l_{max} and k_{max} vs r for the oscillatory modesfor $Pr = \tau$ varying between 10^{-4} and 10^{-7} and $phi = 10^{-3}$. 34

16 Flower Plots obtained by solving equation (51) for λ for Pr = τ= 10^{-6} and $\phi = 0$. 35

17 The Collective Instability and Fingering Instability growth rates for $\phi = 0$. Left: lines with circle markers represent oscillatory modes and solid lines represent the fingering mode. Right: lines with circle markers represent oscillatory modes and solid lines represent the stern number (see equation 59). 36

18 Flower Plots obtained by solving the Equation (51) for λ for $Pr = \tau = 10^{-6}$ and $\phi = 10^{-3}$. Both direct modes (main plot) and oscillatory modes (see inset) are presented. 38

19 λ_{max} for direct modes as a function for r. The lines with circle markers represent turbulent direct modes. The lines with square markers represent laminar modes (i.e. $A_1 = A_2 = 0$ and $Nu = 1$). Solid lines represent the fingering mode when $\phi = 10^{-3}$. 39

20 λ_{max} for direct modes as a function for r at Pr, $\tau = 10^{-7}$ at various ϕ. The solid dark line represents the fingering mode. Lines with markers represent the turbulent case. 40

21 λ_{max} for oscillatory modes as a function for r at $Pr, \tau = 10^{-7}$ at $\phi = 10^{-3}$. The solid lines represent the numerical predictions corresponding to the laminar case. Lines with markers represent the numerical predictions corresponding to the turbulent case. 40

22 A comparison of the diffusion coefficients as a function of R_0. 43

List of Tables

1 Comparison of Coefficients for $Pr = \tau = 10^{-6}$, and $R_0 = 1.2$ $(r \approx 2 \times 10^{-7})$ and $R_0 = 10^5$ $(r \approx .1)$ 36

Abstract:

The Search for Hidden Mixing; Analysis of the Collective and Intrusive Instabilities for Low Prandtl Number and Diffusivity Ratio Systems

by

Michael Medrano

Low mass stars on the red giant branch (RGB) experience more mixing in their outer convection zone than what is predicted by stellar evolution theory. If there exists an inverse composition gradient on the external wing of the HBS shell after the first ‘dredge- up’, then an unstable composition stratification along with the stable stratification played by entropy implies that double diffusive mixing processes should occur in stellar interiors and that some of the hidden mixing might be a result of double diffusive convection. We explore double diffusive modes in the case where there exists a lateral gradient in composition and entropy, in addition to a vertical gradient in order to understand their mixing rates. We find that under these circumstances, the mixing rates of laminar fingering modes and oscillatory modes may be able to address the missing mixing problem. In addition, we find that the ‘collective instability’, oscillatory modes with no lateral gradients cannot explain the missing mixing on the RGB.

Acknowledgements:

Thanks Pascale! Thanks Eireene!

1 Introduction:

1.1 Motivation:

This study seeks to gain a more complete understanding of the mixing processes involved in low mass stars ($.8M_\odot < M < 1.2M_\odot$) as they ascend the red giant branch (RGB). After the star has exhausted all the hydrogen in the core, it continues to fuse hydrogen in a shell surrounding the Helium- rich core. While the core is typically stable to convection, stars on the RGB usually have an outer convection zone located in a shell near the surface. This region is homogeneously mixed.

As time progresses, the hydrogen burning shell (HBS) gets thinner (Charbonnel and Zahn, 2007). Simultaneously, the outer convective envelope expands inwards and mixes roughly 50% of the star by mass in an event called the "First Dredge Up" (Gilroy, 1989). The major elements dredged up from the deep layers into the convective envelope are ^{13}C and ^{14}N- both of which are products of the CNO cycle (Gilroy, 1989). In addition to transporting the products of fusion from deep within the star to the surface, fragile elements such as Li, Be, and B and the primordial ^{12}C are brought down from the surface to the bottom of the convective zone (Gilroy, 1989). Since the temperature of the deepest regions of the convective shell are very hot, the light elements are burned. We observe this event as a drop in the spectral abundances of Li, Be, and B. The ratios $^{12}\mathrm{C}/^{13}\mathrm{C}$ and $^{12}\mathrm{C}/^{14}\mathrm{N}$ also change as a result of the dredge- up event.

After the first dredge up event, the hydrogen burning shell continues to expand outwards- closely following the retreating convective envelope. However, the two regions - the hydrogen burning shell and outer convective envelope- never overlap. As a result, no further changes in surface abundances and isotopic ratios are predicted (Charbonnel and Zahn, 2007). This model is referred to as the canonical stellar evolution theory on the RGB.

The problem with stellar evolution theory along the RGB is that after the first dredge up, the observed isotopic ratios and abundances continue to change dramatically; we would otherwise expect these values to remain constant (Gilroy, 1989, Charbonnel, 1994, Gratton et al., 2000, Dearborn et al., 1975, Charbonnel

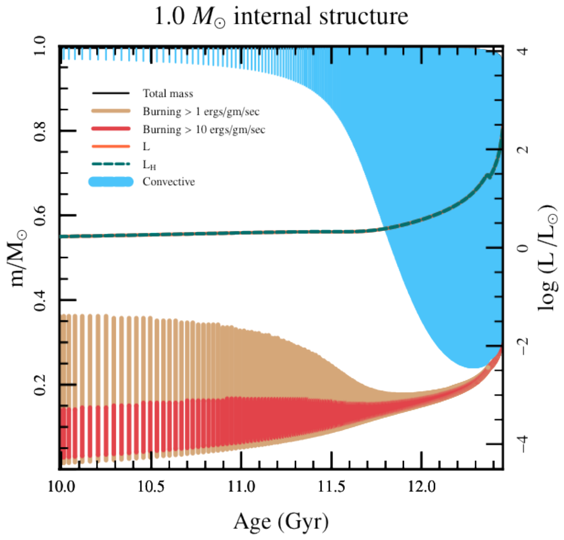

Figure 1: The internal structure of a low mass RGB star. Shortly after the end of the Main Sequence (≈ 10 Gyr), the convective region is restricted to $m/M_\odot \approx 1$. The hydrogen burning shells are located much deep in the star, $m/M_\odot \approx .2$. The "first dredge up" occurs at $t \approx 12.3$ Gyr. The luminosity bump occurs shortly after- marked by the green curve L_H. Courtesy K. Moore.

and Zahn, 2007). Palacios and Brun (2007) point out that no less than 98% of low -mass stars along the RGB exhibit surface abundances which vary sharply from the predicted value. This discrepancy implies that there must be some internal mixing between the convective zone and the hydrogen burning shell that is not accounted for by canonical stellar theory. Numerous studies have been published with the aim of investigating possible mechanisms for mixing along the RGB after the first dredge up.

The possibility that rotation in stars could account for the missing mixing along the RGB has been explored intensely by Sweigart and Mengel (1979), Lattanzio et al. (2006), Wasserburg et al. (1995) - among others. In a more recent paper, Palacios et al. (2006) found that rotation is unable to produce the mixing required to explain the abundance problem in low mass RGB stars.

More recently, Eggleton et al. (2007) investigated a new mixing process they attribute to the presence

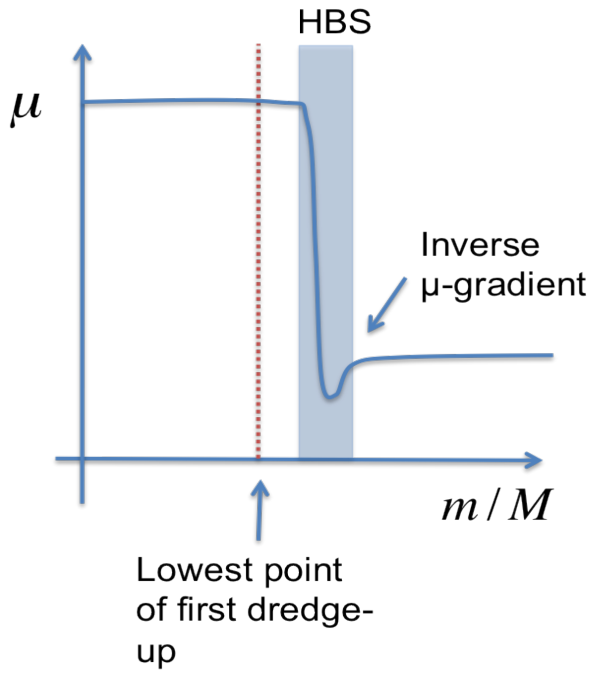

Figure 2: Mean Molecular Weight μ as a function of reduced mass coordinate $m/M_{\odot}$ after HBS moves past lowest point of the first dredge up. We see an inverse μ gradient since $^{3}(^{3}\mathrm{He},2\mathrm{p})^{4}$ is the energetically preferred reaction in the cooler region of the HBS- the HBS region closest to the surface of the star. Courtesy Garaud.

of an inverse molecular weight gradient resulting from the energetically favorable $^{3}(^{3}\mathrm{He},2\mathrm{p})^{4}\mathrm{He}$ pp chain reaction. The final step of the p-p chain is $^{3}\mathrm{He}$ burning, $^{3}\mathrm{He} + {}^{3}\mathrm{He} \rightarrow {}^{1}\mathrm{H} + {}^{1}\mathrm{H} + {}^{4}\mathrm{He}$ reaction - abbreviated as $^{3}(^{3}\mathrm{He},2\mathrm{p})^{4}\mathrm{He}$. This reaction increases the number of particles per unit mass and therefore decreases the mean molecular weight (Ulrich, 1972). Since the portion of the HBS closest to the surface is relatively cool, the dominant reaction in the external wing of the HBS is $^{3}(^{3}\mathrm{He},2\mathrm{p})^{4}$ (Eggleton et al., 2006, 2007, Ulrich, 1972). All other reactions involved in the p-p chain are suppressed. Closer to the core region, the temperature becomes warm enough for all the processes involved in the p-p chain to take place. Restricting our attention to the cooler region in the HBS, we observe a compositionally unstable stratification or inverse μ profile (see Figure 2).

Dearborn et al. (2006) ran 3D simulations to investigate the mixing processes resulting from such an unstable stratification and found that they might help to solve the problem of the observed surface isotopic abundances. They initially attributed the observed mixing to the Rayleigh- Taylor Instability (i.e. the overlaying of dense fluid over light fluid) (Dearborn et al., 2006, Eggleton et al., 2006, 2007). Charbonnel and Zahn (2007) later showed that the system they were referring to is more accurately described by the "thermohaline instability", a double diffusive instability named after a related process that takes place in the ocean and that can occur even when the density is stably stratified. This instability is the subject of this thesis. We discuss the thermohaline instability as well as the related semi- convective instability in the following section.

1.2 Small- Scale Double- Diffusive Instabilities:

Consider some fluid in a 3-dimensional Cartesian coordinate system. Acceleration due to gravity is acting in the $-\hat{\mathbf{e}}_z$ direction. Double diffusive convection occurs when the density of a fluid depends on two or more components which diffuse at different rates. There are two kinds of double diffusive convection: fingering convection (thermohaline convection) and oscillatory double diffusive convection (semi- convection).

Oscillatory double diffusive convection (ODDC), or semi-convection, occurs if the more slowly diffusing component has a stable vertical stratification, whereas the more quickly diffusing component has an unstable stratification. This happens for example in the oceanographic case where heat diffuses much more quickly than salt, whenever both temperature and salinity decrease upward. This situation is commonly found in the polar ocean.

Consider the case illustrated in Figure 3 in which a parcel of water -which has all the properties (i.e. salinity and temperature) of water at its initial vertical position - is perturbed downward. If not for the quickly diffusing component of temperature, this water parcel, perturbed slightly would experience a restoring force back toward its initial position; the reason for this is that its the background density profile is stable. However, if temperature diffusion occurs very rapidly, the water parcel will gain some heat from the environment when perturbed downward. The water parcel will become lighter - when compared to parcels of

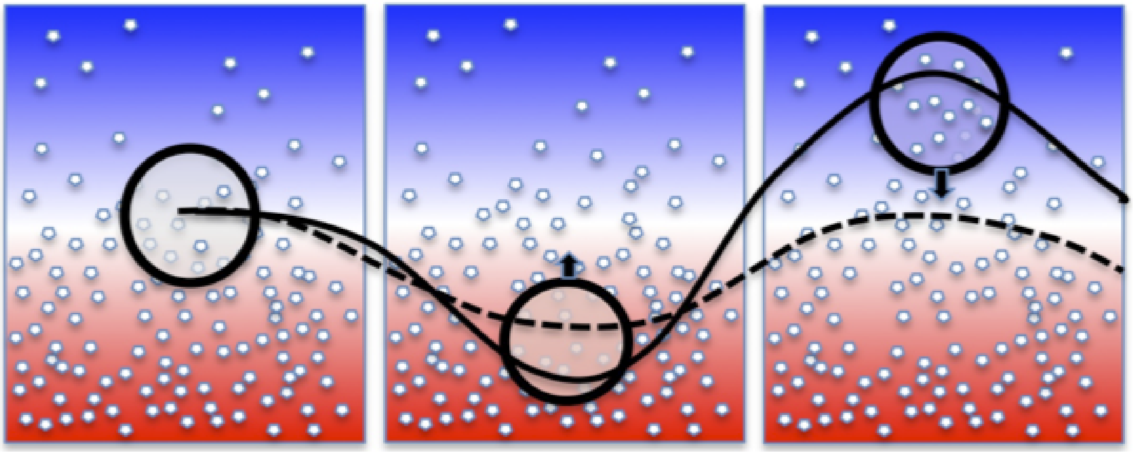

Figure 3: The ODDC Instability. The water parcel (black circle) is perturbed downward. The dotted black line shows the motion of the parcel in the case temperature diffusion is negligible and hence, the density of the parcel is constant. Notice, that in this case, the trajectory is purely oscillatory. The black line shows the case where temperature diffusion occurs much more rapidly than diffusion due to salinity. The result of this process is to amplify amplitude of the wave motion in the vertical. From Garaud (2013)

water at the same height - and begins to rise again. Because the water parcel is lighter than it was prior to the initial perturbation, it overshoots its initial vertical position. It looses some heat to the surrounding environment after overshooting and its density increases again. Since the density of the water parcel increases, the water parcel begins to sink and overshoots further down again. This feedback results in oscillatory motion in the vertical direction with an amplitude that grows exponentially. Although it is useful to understand this process for later, my work will be more concerned with the properties of fingering convection, described below.

Fingering convection (also called thermohaline convection) occurs when the slowly diffusing component has an unstable stratification and the quickly diffusing component has a stable stratification. In the case of salt water, again, this situation commonly occurs in the tropical ocean where warm salty water lies on top of cool fresh water (see Figure 4). If a parcel of water in this system is perturbed downward slightly, and diffusion due to temperature is ignored, again its tendency is to return to its initial vertical position. However, if temperature diffusion occurs very rapidly, heat will be lost by the water parcel. The result of this process is an increase in density of the water parcel relative to its new environment; and, the parcel continues to sink -

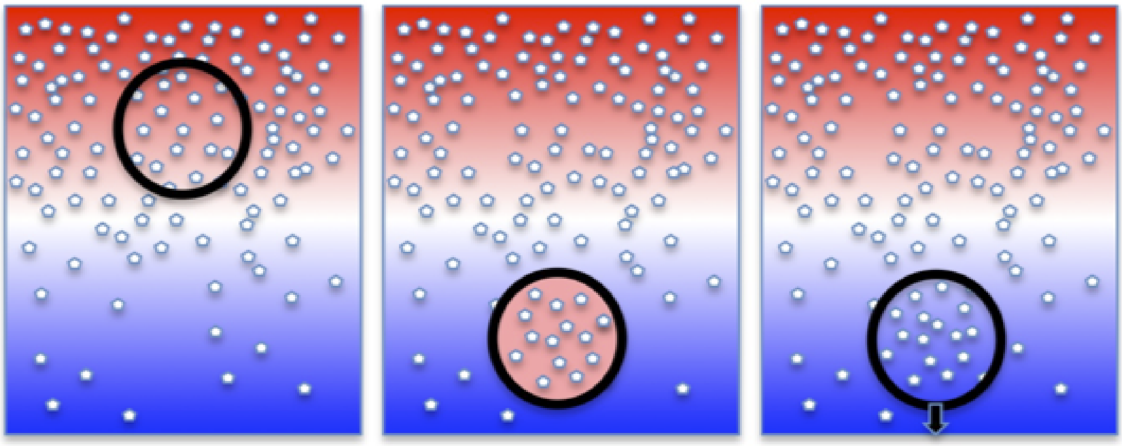

Figure 4: The Basic Fingering Instability. Here a relatively warm and salty water parcel (black circle) is perturbed downward. Since, temperature diffusion occurs very rapidly, the parcel becomes much cooler and hence, denser than neighboring parcel and begins to sink. From Garaud (2013)

forming columns of salty water or “salt fingers". In stars ascending the RGB, the molecular weight inversion caused by changing chemical composition plays the role of the unstable salinity stratification and entropy plays the role of temperature, but the process of the fingering instability is otherwise unchanged. The only difference lies in the typical system parameters (see Section 3.3).

1.3 Mathematical Model of Fingering Instabilities

In order to model a system unstable to fingering convection, we assume a Cartesian coordinate system with gravity acting in the direction $\mathbf{g} = -g\mathbf{e}_z$. We treat the fluid with the Boussinesq approximation (Spiegel and Veronis, 1960). This approximation is valid in the case where the fingering scales are much smaller than the local scale height which is always true in stars and the velocities of the fluid are highly subsonic (Spiegel and Veronis, 1960).

The background temperature and composition profiles are given by $T_0(z) = T_{0z}z$ and $\mu_0(z) = \mu_{0z}z$. The diffusion coefficient due to temperature and molecular weight are κ_T and κ_μ. We represent the viscosity of the fluid by ν. The equation of state is given by:

$$\frac{\rho}{\rho_0} = \alpha T + \beta \mu \tag{1}$$

where ρ_0 is the mean density of the region, ρ is the deviation from the mean, $\alpha = -\partial\rho/\partial T|_{T_0,\mu_0}$- the coefficient corresponding to thermal expansion- and $\beta = \partial\rho/\partial\mu|_{T_0,\mu_0}$ - the coefficient of compositional contraction. To non-dimensionalize the system, we employ the following scales. As in Traxler et al. (2011), we let the length scale be the expected finger scale $\left[l\right] = d = (\kappa_T \nu/g\alpha\left|T_{0z} - T_{0z}^{ad}\right|)^{1/4}$ where T_{0z}^{ad} is the local adiabatic temperature gradient. For time $\left[t\right] = d^2/\kappa_T$, temperature $\left[T\right] = (T_{0z} - T_{0z}^{ad})d$, and composition $\left[\mu\right] = (\alpha/\beta)(T_{0z} - T_{0z}^{ad})d$. The relevant non-dimensional parameters are the Prandtl number $Pr \equiv \nu/\kappa_T$, and the diffusivity ratio $\tau \equiv \kappa_\mu/\kappa_T$. Not that for salt water $Pr \sim 7$ and $\tau \sim 0.01$ while for stars $Pr \sim 10^{-6}$ and $\tau \sim 10^{-6}$.

In studies of fingering or oscillatory double -diffusive convection, the relevant parameter for stability is the density ratio, defined as:

$$R_0 = \frac{\alpha\left(T_{0z} - T_{0z}^{ad}\right)}{\beta\mu_{0z}} = \frac{\nabla - \nabla_{ad}}{\frac{\phi}{\delta}\nabla_\mu} \tag{2}$$

Here, $\nabla = \left(dlnT/dlnP\right)$ is the temperature gradient, $\nabla_{ad} = (dlnT/dlnP)_{ad}$ is the adiabatic temperature gradient, and $\nabla_\mu = (dln\mu/dlnP)$ is the compositional gradient (Kippenhahn et al., 1990). We investigate systems in which $1 < R_0 < 1/\tau$, which are unstable to fingering convection (Baines and Gill, 1969). As in Brown et al. (2013), we will sometimes prefer to use the “reduced density ratio",

$$r = \frac{R_0 - 1}{\tau^{-1} - 1} \tag{3}$$

in which case the instability range is $r \epsilon \left[0, 1\right]$ (Brown et al., 2013). The non-dimensional governing equations for the fingering instability are then given by (Spiegel and Veronis, 1960):

$$\nabla \cdot \mathbf{u} = 0 \tag{4}$$

$$\frac{1}{Pr}\left(\frac{\partial \mathbf{u}}{\partial t} + \mathbf{u} \cdot \nabla \mathbf{u}\right) = -\nabla p + (T - \mu)\hat{\mathbf{e}}_z + \nabla^2 u \tag{5}$$

$$\frac{\partial T}{\partial t} + \mathbf{u} \cdot \nabla T + w = \nabla^2 T \tag{6}$$

$$\frac{\partial S}{\partial t} + \mathbf{u} \cdot \nabla \mu + \frac{w}{R_0} = \tau \nabla^2 \mu. \tag{7}$$

To determine the properties of the fastest growing fingering mode, we linearize these equations assuming solutions of the form:

$$\mathbf{u} = \tilde{\mathbf{u}}(x, y, z, t)$$

$$P(x, y, z, t) = P_0(z) + \tilde{P}(x, y, z, t)$$

$$T(x, y, z, t) = T_0(z) + \tilde{T}(x, y, z, t)$$

$$\mu(x, y, z, t) = \mu_0(z) + \tilde{\mu}(x, y, z, t)$$

where the tilde terms represent small perturbation to the background fields, $P_0(z)$, $T_0(z)$, and $\mu_0(z)$. The background velocity field is assumed to be zero.

Substituting these expressions into the non- dimensionalized momentum equation and throwing away terms that are quadratic in the perturbations gives:

$$\frac{1}{Pr}\left(\frac{\partial \tilde{\mathbf{u}}}{\partial t} + \tilde{\mathbf{u}} \cdot \nabla \tilde{\mathbf{u}}\right) = -\nabla p + (T - \mu)\hat{z} + \nabla^2 \tilde{\mathbf{u}}$$

$$\Rightarrow \frac{1}{Pr}\frac{\partial \tilde{\mathbf{u}}}{\partial t} = -\nabla(p_0 + \tilde{p}) + (T_0 + \tilde{T} - (\mu_0 + \tilde{\mu}))\mathbf{e}_z + \nabla^2 \tilde{\mathbf{u}}$$

$$\Rightarrow \frac{1}{Pr}\frac{\partial \tilde{\mathbf{u}}}{\partial t} = -\nabla \tilde{p} + (\tilde{T} - \tilde{\mu})\hat{z} + \nabla^2 \tilde{\mathbf{u}}$$

as long as $\nabla p_0 + T_0 - \mu_0 = 0$. In this derivation, we have neglected many effects such as temperature dependent viscosity and diffusivity and cross diffusion effects - the case where the molecular diffusion of one substance is affected by the gradient of others (Radko, 2013). In addition, all non- linear effects of double diffusive convection have been completely neglected. For information on these, see Radko (2013).

After linearizing the temperature and chemical composition equations in a similar fashion and discarding the tildes, the linearized governing equations are given by (Spiegel and Veronis, 1960):

$$\nabla \cdot \mathbf{u} = 0 \tag{8}$$

$$\frac{1}{Pr}\frac{\partial \mathbf{u}}{\partial t} = -\nabla p + (T - \mu)\mathbf{e}_z + \nabla^2 \mathbf{u} \tag{9}$$

$$\frac{\partial T}{\partial t} + w = \nabla^2 T \tag{10}$$

$$\frac{\partial \mu}{\partial t} + \frac{w}{R_0} = \tau \nabla^2 \mu. \tag{11}$$

We then assume the velocity, temperature, and composition fields have the form:

$$\left\{u, T, \mu\right\} = \left\{\hat{u}, \hat{T}, \hat{\mu}\right\} exp(\lambda t + mx + ny + kz). \tag{12}$$

where λ is the growth rate of the corresponding mode and m, n, and k are wave numbers associated with axes x, y, and z. We substitute this ansatz into the governing equations (Baines and Gill, 1969). It can be shown that the growth rate of the fingers are independent of the vertical wavenumber k - and so, the terms involving k are discarded here (Radko, 2013). We define $l = \sqrt{n^2 + m^2}$ to be the horizontal wavenumber.

Combining the governing equations results in the following cubic (Baines and Gill, 1969):

$$\lambda^3 + a_2\lambda^2 + a_1\lambda + a_0 = 0 \tag{13}$$

$$a_2 = l^2(1 + Pr + \tau) \tag{14}$$

$$a_1 = l^4(\tau Pr + Pr + \tau) + Pr(1 - R_0^{-1}) \tag{15}$$

$$a_0 = l^6\tau Pr + l^2 Pr(\tau - R_0^{-1}). \tag{16}$$

In order to determine the growth rate λ of the fastest growing mode, we maximize λ with respect to the horizontal wavenumber l (Brown et al., 2013). This results in the following quadratic for λ (Brown et al., 2013):

$$a_2\lambda^2 + a_1\lambda + a_0 = 0 \tag{17}$$

$$a_2 = 1 + Pr + \tau \tag{18}$$

$$a_1 = 2l^2\big(\tau Pr + \tau + Pr\big) \tag{19}$$

$$a_0 = 3l^4\,\tau Pr + Pr\big(\tau - \frac{1}{R_0}\big). \tag{20}$$

Equations (13) and (17) can then be solved simultaneously for λ and l using a Newton- Raphson algorithm to find the fastest growing mode λ_{max} and its corresponding wavenumber l_{max} (Brown et al., 2013).

The Newton Method is rooted in the Taylor series expansion of a function in the neighborhood of a point (Press et al., 1992),

$$f(x + \delta) \approx f(x) + f'(x)\delta + \frac{f''(x)}{2}\delta^2 + ...$$

For small values of δ, and for well- behaved functions, the terms of order δ^2 and above can be neglected (Press et al., 1992). If we let $x_{i+1} = x + \delta$ and $x_i = x$, then the taylor expansion of $f(x)$ can be approximated as:

$$f(x_{i+1}) \approx f(x_i) + f'(x_i)(x_{i+1} - x_i).$$

Since, we would like to know the roots of $f(x)$, we let $f(x_{i+1}) \to 0$ and solve for x_{i+1} given x_i

$$x_{i+1} = x_i - \frac{f(x_i)}{f'(x_i)}.$$

The analogue in the the 2D case is:

$$(x_{i+1}, y_{i+1}) = (x_i, y_i) - \text{Jac}(f(x_i, y_i), g(x_i, y_i))^{-1} \cdot (f(x_i, y_i), g(x_i, y_i)) \tag{21}$$

where Jac refers to the Jacobian of the functions $f(x, y)$ and $g(x, y)$. The algorithm is repeated until the error drops below required tolerance. For our purposes, this tolerance is $O(10^{-14})$. See Press et al. (1992) for more information.

Going back to our original problem of finding its corresponding horizontal wavenumber l_{max}. We simply use the Newton algorithm described above to solve equations (13) and (17) simultaneously. This requires an initial trial guess (λ_0, l_0). The success of the algorithm is highly dependent upon the closeness of the initial guess. The initial trial guess for λ_{max} and l_{max} are taken from Appendix B: Asymptotic Analysis from Brown et al. (2013).

Using this numerical method with the asymptotic guesses, we are able to reproduce Figure 13 from Brown et al. (2013) - which overlays their semi- analytical predictions on top of the numerical solution for λ_{max} as a function of the reduced density ratio r (see eq (3)) for values values of Pr and τ. We find that the fingering growth rate λ_{max}, goes to zero as $r \to 1$ or equivalently, as $R_0 \to 1/\tau$- which is the point of marginal stability. This is consistent with what we would expect by directly examining the marginal stability of the cubic (13) instead. Indeed, at marginal stability, $\lambda = 0$. Equation (13) reduces to $a_0 = 0$. Maximizing this expression, with respect to the horizontal wavenumber l gives the result: $R_0 = 1/\tau$ when $\lambda \to 0$.

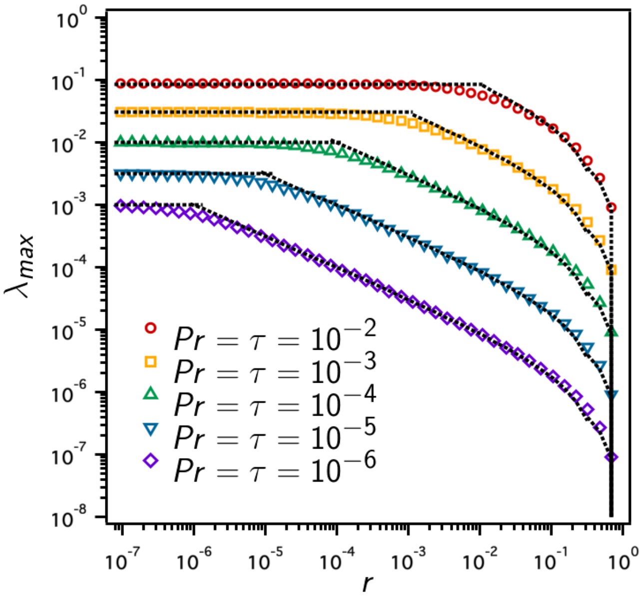

Figure 5: A comparison of the numerical and asymptotic values of the growth rate λ as a function of r.

Our ultimate goal is to understand how much mixing can arise from double- diffusive instabilities. The efficiency of mixing is often measured through the Nusselt number, defined as the ratio of the total flux (turbulent + diffusive flux) to the diffused flux or

$$Nu_T = \frac{-\frac{dT}{dz}\kappa_T + F_T}{-\frac{dT}{dz}\kappa_T} = 1 - \hat{F}_T. \tag{22}$$

where $\hat{F}_T$ is the non- dimensional turbulent flux. Dimensional analysis of the governing equations implies that the Nusselt Number can only be a function of R_0, τ, and Pr. Brown et al. (2013) found that a good estimate for the thermal and compositional Nusselt numbers at low Prandtl number and diffusivity ratio are given by:

$$Nu_T = 1 + C^2 \frac{\lambda_{max}^2}{l_{max}^2(\lambda_{max} + l_{max}^2)} \tag{23}$$

$$Nu_{\mu} = 1 + C^2 \frac{\lambda_{max}^2}{\tau l_{max}^2(\lambda_{max} + \tau l_{max}^2)} \tag{24}$$

where $C = 7$.

Using Equation (24) then leads to a total effective flux for composition as:

$$\begin{aligned} F_{\mu}^{total} &= -Nu_{\mu}\kappa_{\mu}\frac{d\overline{\mu}}{dz} \\ &= -\kappa_{\mu,\,turb}\frac{d\overline{\mu}}{dz} \end{aligned}$$

where $\kappa_{\mu,\,turb} = Nu_{\mu}\kappa_{\mu}$. Figure 6 shows Nu_{μ} as a function of R_0 for $Pr = \tau = 10^{-6}$ based on the Brown et al. (2013) model.

Traxler et al. (2011), Brown et al. (2013), and Denissenkov and Merryfield (2011), argued that the mixing resulting from thermohaline or fingering convection cannot explain the missing mixing on the RGB. Indeed, as shown in Figure 6, Brown et al. (2013)'s model implies a thermohaline mixing rate which is a factor of 100 smaller than the observationally required rate of RGB extra-mixing. In this work we explore the possibility that thermohaline convection may excite additional double diffusive instabilities - such as the collective and intrusive instability. Perhaps, by including these new instabilities, we may be able to explain the missing mixing along the RGB.

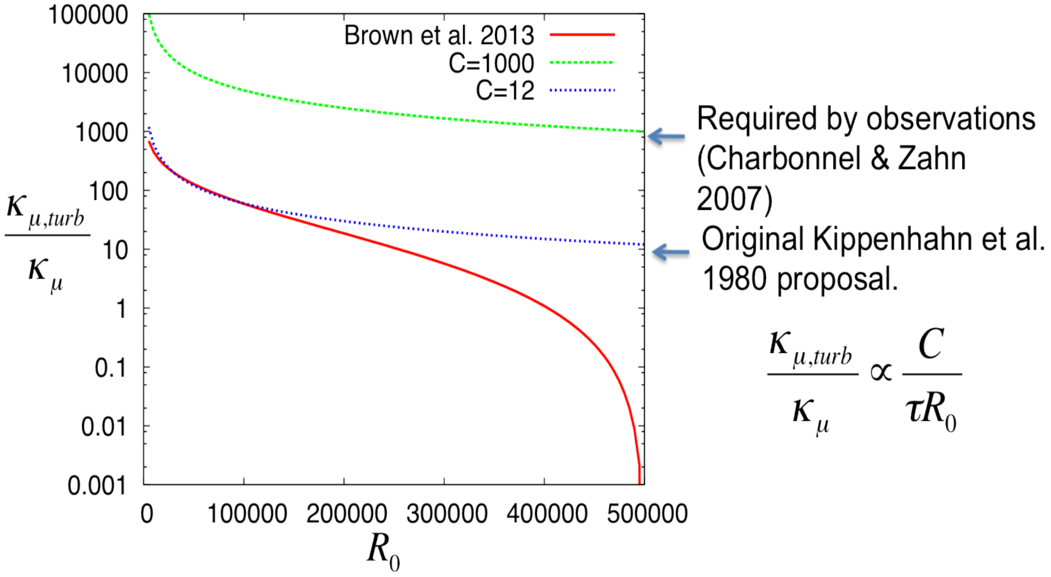

Figure 6: A comparison of the Nu_0 corresponding to fingering convection with Nu_0 required by observations in order to explain the missing mixing problem along the *RGB*. Courtesy Garaud.

2 Large Scale Double Diffusive Instabilities

2.1 The collective and intrusive instabilities

Rather than discuss the instability of a single finger, one could instead discuss the "collective instability" of many fingers. Again for pedagogical purposes we consider the simple oceanic case of salt water although similar instabilities exist in stellar interiors as well. To understand the mechanism for the collective instability more completely, let's "zoom out" of the small- scale fingering regime - in which $\kappa_T \gg \kappa_\mu$ - and observe the system with this new large scale perspective. We see many salt fingers "falling" in the vertical direction as opposed to just one salt finger. In this turbulent or "zoomed- out" perspective, the compositional flux is much greater than the flux due to temperature - that is $\kappa_{\mu,turb} \gg \kappa_{T,turb}$. Recall from section 3.2, if the quickly diffusing component has an unstable background stratification, the system is unstable to semi- convection or ODDC instead of fingering. In the turbulent regime, salinity is the more quickly diffusing component of density but still has an unstable background stratification - since salty water is overlaying fresher water. Therefore, from a turbulent perspective, the system produces internal waves whose components - rather than microscopic water parcels - are patches of fingers. This phenomenon is known as the "collective instability"; however, the mechanism described is really ODDC.

Another common large-scale instability is that of intrusions. One property that all intrusions have in common is that they are excited only when there exists a lateral gradient of temperature and salinity in the system, in addition to the vertical gradients previously discussed (see Section 4.2) (Radko, 2013). The mixing that results from intrusions is sometimes referred to as "direct" since intrusions consistently transfer warm, salty fluid laterally into colder, fresher regions and vice- versa (Radko, 2013), while in the collective instability the fluid flow periodically changes direction. The picture describing the intrusive instability is as follows.

Consider the system in Figure 7. The fronts of the intrusive currents and temperature and salinity contours are tilted such that they are sloping downward in the positive x - direction (Radko, 2013). The intrusions are less tilted than the isotherms and isohalines (Radko, 2013). As a result, the upward mov-

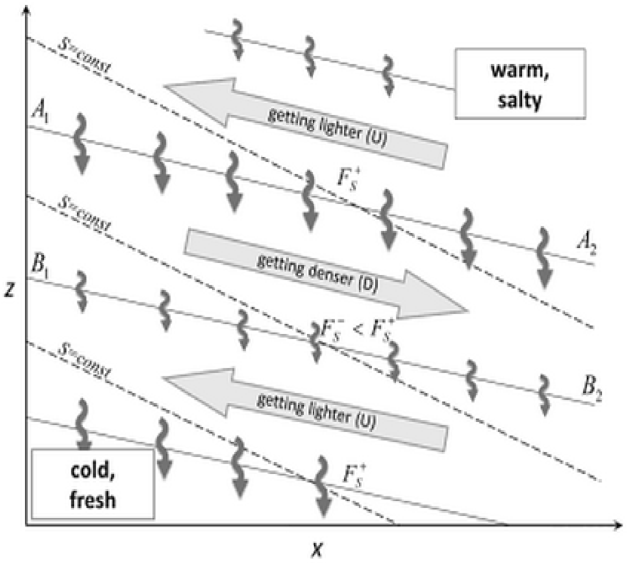

Figure 7: The Intrusive Instability. The dotted lines correspond to the mean isohalines. Although the isotherms are not shown, there slope very close follows the isohalines. From Radko (2013)

ing flow or (intrusions) transports warm, salty water across isohalines and isotherms to cold, fresh regions (Radko, 2013).

This fluid advection results in a local increase of temperature and salinity, in the region where the fluid was advected to. In contrast, the downward flows or intrusions reduce the local salinity and temperature since they advect cold, fresh water across isotherm and isohalines to regions of warm, salty water (Radko, 2013). We find that in regions below the upward intrusions and above the downward moving intrusions, the fluid flow the gradient of the local temperature, salinity stratifications - thus, increasing the vertical flux of fingers. In regions below the downward intrusions, but above the upward moving intrusions, the background gradients are reduced - the result of which is to decrease the vertical flux of the fingers. This leads to appositive feedback loop which promotes the exponential growth of the instability.

Intrusions and the collective instability waves share many qualities. Both of these instabilities are driven by a feedback loop in which the advection of some fluid alters the local density and temperature stratifications and thus enhancing or diminishing the vertical flux of fingers. A major difference between these modes is that the intrusions require a lateral gradient to exist, while the “Collective Instability” does not (Radko, 2013).

2.2 Unified Mathematical Model for Double Diffusive Instabilities

In the presence of lateral temperature and chemical composition gradients, Traxler et al. (2011) proposed a unified formalism to study, at the same time, standard instabilities (fingering instability, and ODDC), as well as, collective instabilities (turbulent intrusions and gravity waves). We reproduce their derivation here.

The dimensional background temperatures and composition profiles are now given by $T_0(x,z) = T_{0x}x + T_{0z}z$ and $\mu_0(x,z) = \mu_{0x}x + \mu_{0z}z$. As in Traxler et al. (2011), we assume that the total background horizontal density gradient to be zero, which implies $\alpha T_{0x} - \beta\mu_{0x} = 0$ Traxler et al. (2011). We refer to the slope of the background temperature gradient $\phi = T_{0x}/T_{0z}$, as the non-dimensional lateral gradient.

In the presence of lateral temperature and compositional gradients, the non-dimensional equations for the evolution of the velocity, temperature, and composition fields, respectively $\mathbf{u} = (u,v,w)$, $T(x,y,z,t)$, and $\mu(x,y,z,t)$ are (Traxler et al., 2011):

$$\frac{1}{Pr}\left(\frac{\partial \mathbf{u}}{\partial t} + \mathbf{u}\cdot\nabla\mathbf{u}\right) = -\nabla p + (T-\mu)\hat{\mathbf{e}}_z + \nabla^2\mathbf{u}, \tag{25}$$

$$\nabla\cdot\mathbf{u} = 0, \tag{26}$$

$$\frac{\partial T}{\partial t} + \phi u + w + \mathbf{u}\cdot\nabla\mathbf{T} = \nabla^2 T, \tag{27}$$

$$\frac{\partial \mu}{\partial t} + \phi u + \frac{1}{R_0}w + \mathbf{u}\cdot\nabla\mu = \tau\nabla^2\mu. \tag{28}$$

To model the collective effect of many fingers in driving large- scale instabilities, we use a mean field theory, which assumes a separation of scales between the large- scale turbulent modes and the small- scale fingering structures. We define:

$$\mathbf{u}(x,y,z,t) = \bar{\mathbf{u}}(x,y,z,t) + \mathbf{u}'(x,y,z,t) \tag{29}$$

$$T(x,y,z,t) = \bar{T}(x,y,z,t) + T'(x,y,z,t) \tag{30}$$

$$\mu(x,y,z,t) = \bar{\mu}(x,y,z,t) + \mu'(x,y,z,t) \tag{31}$$

where $\overline{\mathbf{u}}$, $\overline{T}$, and $\overline{\mu}$ are averages and $\mathbf{u}'$, T' and μ' are perturbations. The averaging process (denoted by a bar sign: $\overline{...}$) is defined by the following rules:

$$\overline{\overline{\mathbf{u}}} = \overline{\mathbf{u}} \tag{32}$$

$$\overline{\mathbf{u}'} = 0 \tag{33}$$

Typically, we will think of the averaging process as a local spatio- temporal average over many fingers.

Making the substitution $\mathbf{u} = \overline{\mathbf{u}} + \mathbf{u}'$ and similarly for temperature and composition into the momentum equation gives:

$$\frac{1}{Pr}\left(\frac{\partial \overline{\mathbf{u}}}{\partial t} + \frac{\partial \mathbf{u}'}{\partial t} + (\mathbf{u} + \mathbf{u}') \cdot \nabla(\overline{\mathbf{u}} + \mathbf{u}')\right) = -\nabla \overline{P} + (\overline{T} + T' - \overline{\mu} - \mu')\hat{\mathbf{e}}_z + \nabla^2 \overline{\mathbf{u}} + \nabla^2 \mathbf{u}'$$

Expanding the third term on the L.H.S gives:

$$\frac{1}{Pr}\left(\frac{\partial \overline{\mathbf{u}}}{\partial t} + \frac{\partial \mathbf{u}'}{\partial t} + \overline{\mathbf{u}} \cdot \nabla \overline{\mathbf{u}} + \overline{\mathbf{u}} \cdot \nabla \mathbf{u}' + \mathbf{u}' \cdot \nabla \overline{\mathbf{u}} + \overline{\mathbf{u}} \cdot \nabla \mathbf{u}'\right)$$
$$= -\nabla \overline{P} + (\overline{T} + T' - \overline{\mu} - \mu')\hat{\mathbf{e}}_z + \nabla^2 \overline{\mathbf{u}} + \nabla^2 \mathbf{u}'$$

In order to proceed, we must assume that the averaging process commutes with time and spatial derivatives (hence the need for scale separation). Applying the averaging process on the previous expression gives:

$$\frac{1}{Pr}\left(\frac{\partial \overline{\mathbf{u}}}{\partial t} + \overline{\mathbf{u}} \cdot \nabla \overline{\mathbf{u}} + \overline{\mathbf{u}' \cdot \nabla \mathbf{u}'}\right) = -\nabla \overline{p} + (\overline{T} - \overline{\mu})\hat{\mathbf{e}}_z + \nabla^2 \overline{\mathbf{u}}$$

After moving the third term on the L.H.S to the right and defining the Reynold's Stress term: $R_{ij} = \overline{u_i' u_j'}$, the momentum equation becomes:

$$\frac{1}{Pr}\left(\frac{\partial \overline{\mathbf{u}}}{\partial t} + \overline{\mathbf{u}} \cdot \nabla \overline{\mathbf{u}}\right) = -\nabla \overline{p} + (\overline{T} - \overline{\mu})\hat{\mathbf{e}}_z + \nabla^2 \overline{\mathbf{u}} - \frac{1}{Pr}\nabla \cdot \mathbf{R} \tag{34}$$

Similarly, we obtain expressions for temperature and chemical composition:

$$\frac{\partial \overline{T}}{\partial t} + \phi \overline{u} + \overline{w} + \overline{\mathbf{u}} \cdot \nabla \overline{\mathbf{T}} = \nabla^2 \overline{T} - \nabla \cdot \mathbf{F}_T \tag{35}$$

$$\frac{\partial \overline{\mu}}{\partial t} + \phi \overline{u} + \frac{1}{R_0}\overline{w} + \overline{\mathbf{u}} \cdot \nabla \overline{\mu} = \tau \nabla^2 \overline{\mu} - \nabla \cdot \mathbf{F}_\mu \tag{36}$$

where $\mathbf{F_T} \equiv \overline{\mathbf{u}' T'}$ and $\mathbf{F}_\mu \equiv \overline{\mathbf{u}' \mu'}$.

These equations show that in order to evolve the large scale fields $\overline{\mathbf{u}}$, $\overline{T}$, and $\overline{\mu}$ in time and space, we need to be able to express the turbulent fluxes of heat, $\mathbf{F_T}$, chemical composition $\mathbf{F}_\mu$ and, momentum $\mathbf{R}$ in terms of the large scale quantities, but these are a priori known only in terms of the small- scale perturbations. This is a standard closure problem for turbulence. Traxler et al. (2011) addressed the closure problem by neglecting the momentum flux $\mathbf{R}$ and by assuming that most of the temperature and compositional flux is in the vertical direction so that,

$$\nabla \cdot \mathbf{F}_T \approx \frac{dF_T}{dz}$$
$$\nabla \cdot \mathbf{F}_\mu \approx \frac{dF_\mu}{dz}.$$

The motivation for this approximation stems from the fact that the fingers transport material principally in the vertical direction.

For fixed Pr and τ, the Nusselt number is a function of only R_ρ- the local background density- which is defined as:

$$R_\rho = \frac{\alpha T_{0z}(1 + \partial\overline{T}/\partial z)}{\beta\mu_{0z}\left[1 + \left(\frac{\alpha T_{0z}}{\beta\overline{\mu}_{0z}}\right)\partial\overline{\mu}/\partial z\right]} = R_0\frac{1 + \partial\overline{T}/\partial z}{1 + R_0\partial\overline{\mu}/\partial z}. \tag{37}$$

Now, recall the Nusselt number is defined as the ratio of the total flux to the diffused flux or $Nu_T = \frac{-\frac{d\overline{T}}{dz}+F_T}{-\frac{d\overline{T}}{dz}}$. Solving for the flux due to temperature gives: $F_T = (1 - Nu)(1 + \frac{d\overline{T}}{dz})$. The vertical derivative of this quantity is then given by:

$$\begin{aligned} -\frac{dF_T}{dz} &= -\left(\frac{\partial^2\overline{T}}{\partial z^2} - \frac{\partial Nu}{\partial z} - \frac{\partial Nu}{\partial z}\frac{\partial\overline{T}}{\partial z} - Nu\frac{\partial^2\overline{T}}{\partial z^2}\right) \\ &= \frac{\partial Nu}{\partial z} + \frac{\partial Nu}{\partial z}\frac{\partial\overline{T}}{\partial z} + (Nu - 1)\frac{\partial^2\overline{T}}{\partial z^2} \end{aligned} \tag{38}$$

To find dNu/dz, we Taylor expand the Nusselt Number and flux ratio about R_0:

$$Nu(R_\rho) = Nu(R_0) + (R_\rho - R_0)\left.\frac{dNu(R_\rho)}{dR_\rho}\right|_{R0} + ...$$

Then,

$$\frac{dNu}{dz} = \frac{dR_\rho}{dz}\frac{dNu(R_0)}{dR_\rho}$$

Taylor expanding the density ratio and throwing the nonlinear terms away gives:

$$\begin{aligned} R_\rho &= R_0 \frac{1 + \frac{d\overline{T}}{dz}}{1 + R_0 \frac{d\overline{\mu}}{dz}} \\ &\approx R_0\big(1 + \frac{d\overline{T}}{dz}\big(1 - R_0 \frac{d\overline{\mu}}{dz}\big)\big) \\ &\approx R_0\big(1 + \frac{d\overline{T}}{dz} - R_0 \frac{d\overline{\mu}}{dz}\big). \end{aligned} \tag{39}$$

The derivative of the local density ratio with respect to the z- direction is then:

$$\frac{dR_\rho}{dz} = R_0\big(\frac{\partial^2 \overline{T}}{\partial z^2} - R_0 \frac{\partial^2 \overline{\mu}}{\partial z^2}\big) \tag{40}$$

Substituting into eq (38) finally yields:

$$-\frac{dF_T}{dz} = A_2\big(\frac{\partial^2 \overline{T}}{\partial z^2} - R_0 \frac{\partial^2 \overline{\mu}}{\partial z^2}\big) + (Nu_0 - 1)\frac{\partial^2 \overline{T}}{\partial z^2} \tag{41}$$

where

$$A_2 = \frac{dNu_0}{dR_\rho} R_0 \tag{42}$$

and $Nu_0 = Nu(R_0)$. A similar calculation can be done for the compositional flux F_μ and yields

$$-\frac{dF_s}{dz} = A_1(Nu_0 - 1)\big(\frac{\partial^2 T}{\partial z^2} - R_0 \frac{\partial^2 \mu}{\partial z^2}\big) - \frac{1}{\gamma_0}\frac{dF_T}{dz} \tag{43}$$

where,

$$A_1 = R_0 \frac{d\gamma_0^{-1}}{dR_\rho} \tag{44}$$

and $\gamma_0^{-1} = \gamma_{turb}^{-1}(R_0)$ and where we have defined a turbulent flux ratio as

$$\gamma_{turb} = F_T/F_\mu = \frac{R_0(Nu_T - 1)}{\tau(Nu_\mu - 1)}. \tag{45}$$

The coefficients A_1 and A_2 can be found numerically by letting:

$$\frac{dNu_0}{dR_\rho} \approx \frac{Nu_T(R_0+\epsilon) - Nu_T(R_0)}{\epsilon} \tag{46}$$

$$\frac{d\gamma_0^{-1}}{dR_\rho} \approx \frac{\gamma_{turb}^{-1}(R_0+\epsilon) - \gamma_{turb}^{-1}(R_0)}{\epsilon} \tag{47}$$

where ϵ is taken to be some small number.

To summarize, the governing equations describing the large scale fields $\overline{u}$, $\overline{T}$, and $\overline{\mu}$ are given by:

$$\frac{1}{Pr}\left(\frac{\partial \overline{\mathbf{u}}}{\partial t} + \overline{\mathbf{u}} \cdot \nabla \overline{\mathbf{u}}\right) = -\nabla \overline{p} + (\overline{T} - \overline{\mu})\hat{\mathbf{e}}_z + \nabla^2 \overline{\mathbf{u}} \tag{48}$$

$$\frac{\partial \overline{T}}{\partial t} + \phi \overline{u} + \overline{w} + \overline{\mathbf{u}} \cdot \nabla \overline{\mathbf{T}} = \nabla^2 \overline{T} - \frac{dF_T}{dz} \tag{49}$$

$$\frac{\partial \overline{\mu}}{\partial t} + \phi \overline{u} + \frac{1}{R_0}\overline{w} + \overline{\mathbf{u}} \cdot \nabla \overline{\mu} = \tau \nabla^2 \overline{\mu} - \frac{dF_\mu}{dz} \tag{50}$$

where $-dF_T/dz$ and $-dF_\mu/dz$ are given by eqs. (42) and (44). We recover the equations given in Traxler et al. (2011). Note that if $-dF_T/dz = 0$ and $-dF_\mu/dz = 0$, and letting $\overline{\mathbf{u}} \rightarrow \mathbf{u}$, $\overline{T} \rightarrow T$, and $\overline{\mu} \rightarrow \mu$, we recover the equations for the small scale instabilities in the presence of a lateral gradient ϕ. In this sense, this formalism has the advantage of providing a unified view of all possible instabilities in the system, both on the small scale and on large scales. A standard linear stability analysis assuming fields of the form $\{\mathbf{u}, T, S\} = \{\hat{\mathbf{u}}, \hat{T}, \hat{S}\} exp(\lambda t + i(mx + ly + kz))$ results in the cubic:

$$\lambda^3 + a_2\lambda^2 + a_1\lambda + a_0 = 0 \tag{51}$$

where the coefficients are:

$$a_2 = |\mathbf{k}|^2(1 + Pr + \tau) + k^2[(1 - A_1R_0)(Nu_0 - 1) + A_2(1 - \frac{R_0}{\gamma_0})] \tag{52}$$

$$\begin{aligned} a_1 = {} & |\mathbf{k}|^4(\tau Pr + \tau + Pr) + k^2|\mathbf{k}|^2[(\tau + Pr)(A_2 + Nu_0 - 1) \\ & - A_2(1 + Pr)\frac{R_0}{\gamma_0} - A_1R_0(1 + Pr)(Nu_0 - 1)] - k^4A_1R_0(Nu_0 - 1)^2 \\ & + Pr\frac{l^2 + m^2}{|\mathbf{k}|^2}(1 - \frac{1}{R_0}) \end{aligned} \tag{53}$$

$$\begin{aligned} a_0 = {} & |\mathbf{k}|^6\tau Pr + k^2|\mathbf{k}|^4Pr[(\tau - A_1R_0)(Nu_0 - 1) + A_2(\tau - \frac{R_0}{\gamma_0})] \\ & - k^4|\mathbf{k}|^2PrR_0A_1(Nu_0 - 1)^2 + Pr\frac{l}{|\mathbf{k}|^2}\Bigg[|\mathbf{k}|^2[l\frac{l^2 + m^2}{l^2}(\tau - \frac{1}{R_0}) \\ & - k\phi(\tau - 1)] + k^2A_1(1 - R_0)(Nu_0 - 1)(l\frac{l^2 + m^2}{l^2} - k\phi) - k^2[A_2(1 - R_0) \\ & + Nu_0 - 1][l\frac{l^2 + m^2}{l^2}(\frac{1}{R_0} - \frac{1}{\gamma_0}) - k\phi(1 - \frac{1}{\gamma_0})]\Bigg] \end{aligned} \tag{54}$$

where $|\mathbf{k}|^2 = k^2 + l^2 + m^2$. Here, λ is the growth rate of the corresponding mode and m, l, and k are wave numbers associated with axes x, y, and z. Solving the cubic expression (51) results in three solutions for the growth rate λ; there are either three real roots, or one real root and two complex- conjugate roots. Of these three solutions, we are interested in the one with the largest $Re(\lambda)$; all other modes are exponentially smaller after some time interval t. In addition, solutions whose $Re(\lambda) < 0$ are also discarded since as $t \rightarrow \infty$, $exp(\lambda t + imx + ily + ikz) \rightarrow 0$. Solutions with non-zero imaginary part corresponds to oscillatory modes (e.g. the collective instability, internal gravity waves). Solutions with zero imaginary part correspond to direct modes (e.g. the fingering or intrusive instabilities). As discussed above, we recover the fingering cubic (11) by letting $A_1 = A_2 = \phi = 0$ and $Nu = 1$ (Traxler et al., 2011).

The regime of wave numbers at which these instabilities occur can be presented in the form of “Flower

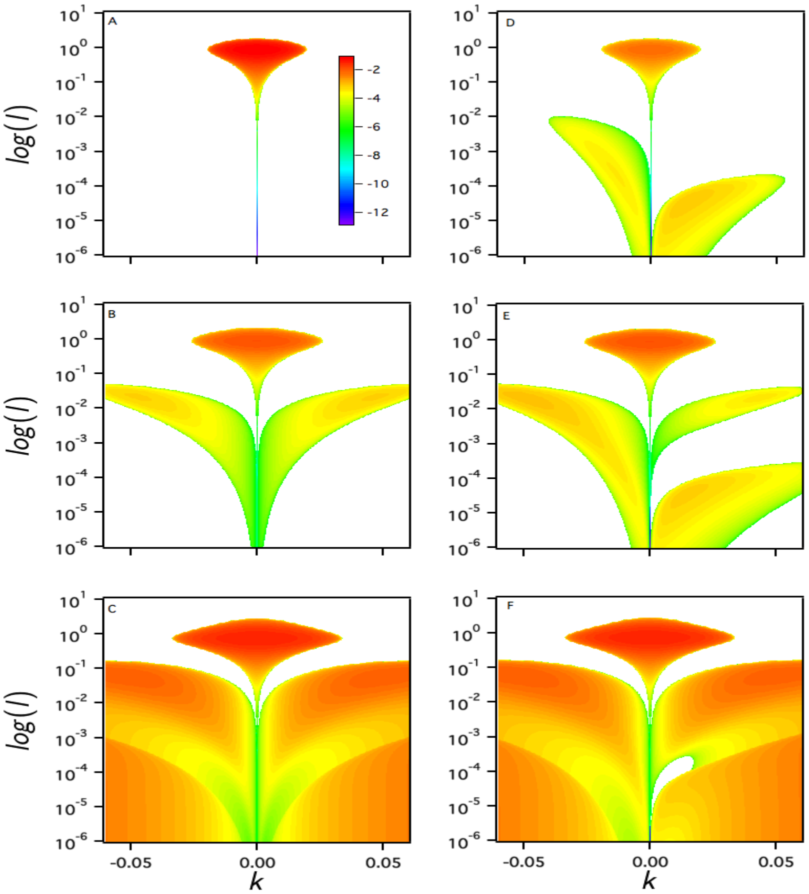

Figure 8: Flower Plots obtained by solving Equation (51) for λ for $Pr = 7$, $\tau = .01$ at (a) $R_0 = 7$, (b) $R_0 = 4.0$, (c) $R_0 = 1.5$. $\phi = 0/.01$ in the left/right columns. This figure recovers Figure 4 of Traxler et al. (2011).

Plots". Typical flower plots for salt water instabilities are shown in Figure 8 and reproduce the results of Traxler et al. (2011). The left column corresponds to $\phi = 0$ and the right column to $\phi = 0.01$. From top to bottom, the density ratio of the system decreases and is therefore more and more unstable. The colors represents the real part of the growth rate, or $Re(\lambda)$, for growing modes. Modes with $Re(\lambda) < 0$ are shown in white.

In the left plots, Figure 8a is for high R_0. Here, only the fingering modes are excited in a “bulb” at relatively large l. In Figure 8b, oscillatory modes appear as “leaves” spanning a large range in l. In Figure 8c; in addition to the bulb and oscillatory modes, we see the layering instability is supported (Radko, 2013).

In the right plots - where $\phi = 10^{-3}$ - Figure 8d we observe that the many modes are supported in this system. A bulb is observed for large l, oscillatory modes for the “leaf” where $k < 0$. The “fatter” leaf represents an intrusive instability. In Figure 8e we observe an oscillatory mode for $k < 0$ as well as in the case $k > 0$ and $l > 10^{-3}$. Again an intrusive mode is observed for low l for $k > 0$. In Figure 8f we observe again layering instabilities “umbrellaed” by oscillatory modes.

Comparing the cases with and without lateral gradients, we see that the latter alter the spectrum of wave numbers at which the second order instabilities are excited. While this calculation was done for salt water parameters, we now apply this to identify all possible modes of instability in the stellar parameter regime.

3 Results:

3.1 The Laminar Case: Oscillatory and Intrusive modes at $\phi = 10^{-3}$

We first set the flux coefficients, $A_1, A_2 = 0$ and $Nu_0 = 1$ in order to learn the about the properties of the fastest growing unstable mode as a function of wave numbers l and k in the case of laminar fluid motion. Recall, under these conditions, if in addition, $\phi \to 0$, we recover the fingering equations (13) discussed earlier. We now study the more general case of laminar fluid motion when a lateral gradient exists; that is, when $\phi \neq 0$.

3.1.1 Intrusions

Figure 9 shows the growth rate of direct modes ($Im(\lambda) = 0$) at Pr $= \tau = 10^{-6}$ for various R_0. As R_0 increases, we see that all of the direct modes retreat to the region where $k < 0$.

To our knowledge this phenomenon in the salt water system has been reported by Walsh and Ruddick (2000) and Radko (2013), but attributed exclusively to variations in the flux ratio $\gamma = F_T/F_S$ with the local density ratio R_ρ (see Section 5.3). We are unaware of any work published about this phenomenon in the case of laminar fluid flow.

At $R_0 = 2 \times 10^4$, we find that, $k_{max} \approx -.5$ and $l_{max} \approx .3$. These wave numbers correspond to small scales that are similar to the basic finger scale, but in contrast with the fingers (which are mostly vertical) these modes are inclined. Another interesting feature in Figure 9, is that unlike the salty water case, the boundaries in wave space between the fingering and intrusive modes are unclear. According to the numerical predictions of equation (52) in the astrophysical regime, there appears to be a continuous spectrum in l in which direct modes can be excited.

Figure 10 shows the growth rate λ_{max} of the fastest growing direct mode overlaid with the fastest fingering growth rates (i.e. when $\phi = 0$) as a function of the reduced density ratio (see equation 3) at various Pr and τ. These plots are constructed by producing flower plots for various $R_0 > 1$ (or $r > 0$) then determining

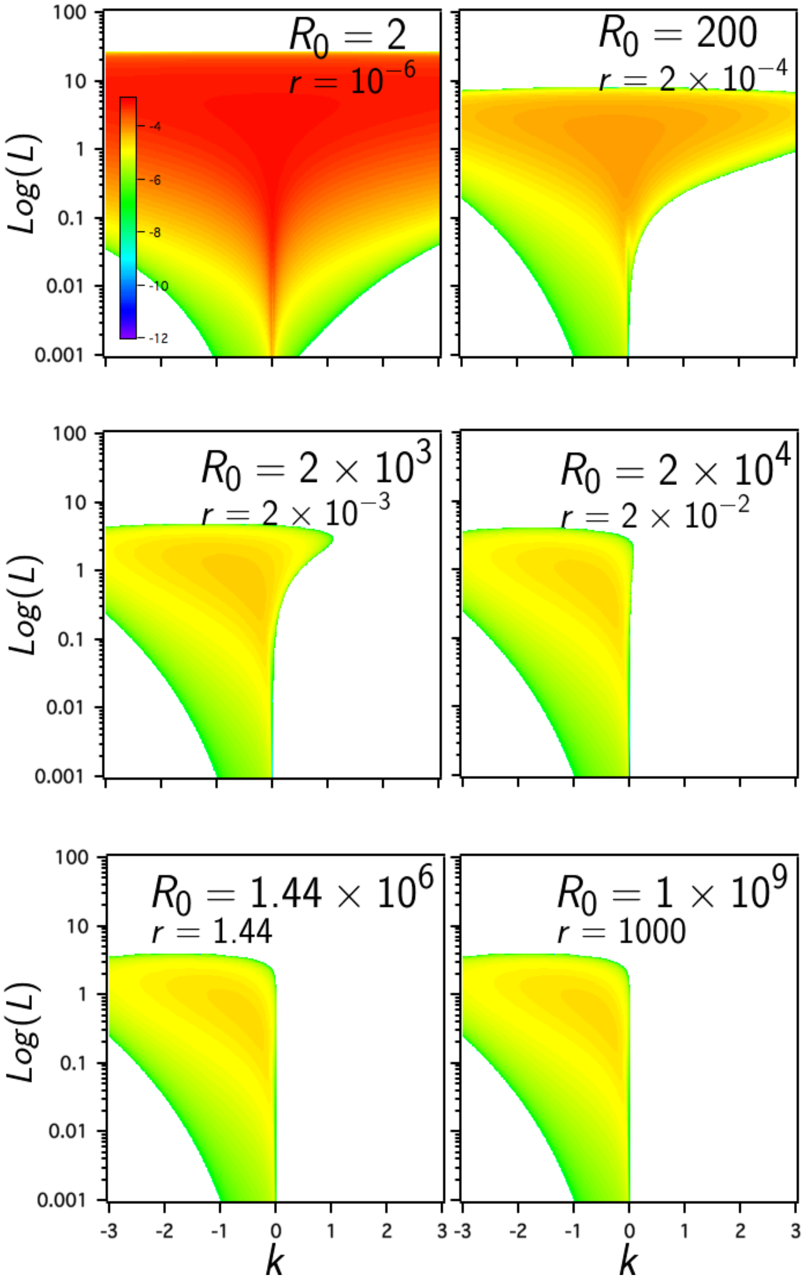

Figure 9: Flower Plots for $Pr = \tau = 10^{-6}$ and $\phi = 10^{-3}$ at various R_0 ($A_1 = A_2 = 0$ and $Nu_0 = 1$). An effect of increasing R_0 is that the intrusive mode is only supported for negative k.

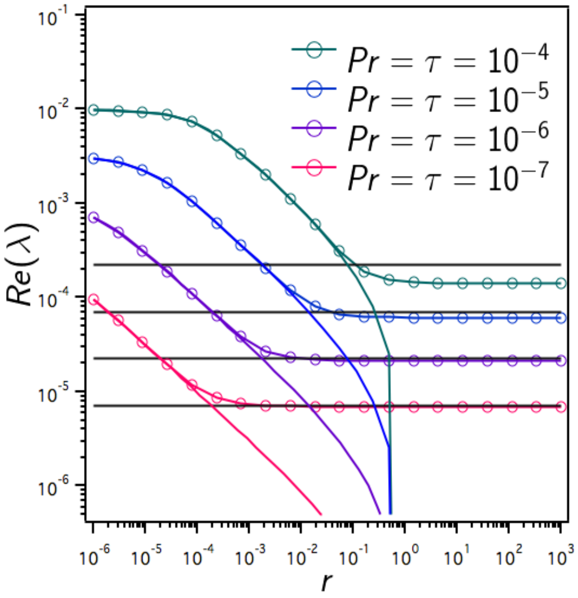

Figure 10: λ_{max} of direct modes as a function of r. The fingering modes are represented by colored solid lines. These have the distinct feature that $\lambda_{max} \to 0$ as $r \to 1$. λ_{max} for the direct modes with $\phi \neq 0$ are depicted by lines with markers.

the largest growth rate of each among all unstable modes with $Im(\lambda) = 0$. Despite the fact that the fingering region exists only for $r \epsilon [0, 1]$ in the $\phi = 0$ case, the intrusive modes in the case $\phi = 10^{-3}$ exist for all values of r, even when $r \to \infty$. In other words, we find that intrusive modes persist even in systems stable to fingering convection, for all density ratios.

To understand the mechanism responsible for this laminar intrusive instability, consider the case in Figure 11 where $R_0 > 1/\tau$ and so, the system is fingering stable. Again, we consider the ocean water case for pedagogical purposes. Since, $R_0 > 1/\tau$, perturbing the water parcel vertically slightly will not cause the fingering mechanism to occur. However, if the water parcel is perturbed laterally over -say decreasing isotherms and isohalines, the water parcel will be relatively warmer/saltier than neighboring parcels. Since, $\kappa_T \gg \kappa_\mu$, heat diffuses away from the parcel rapidly. The parcel is now denser than its surrounding neighbors and sinks. Although the parcel “falls” in the vertical, its total trajectory is actually some angle with respect to the horizontal instead. We see the total trajectory at which the fingers fall is given by the dotted line in Figure 11.

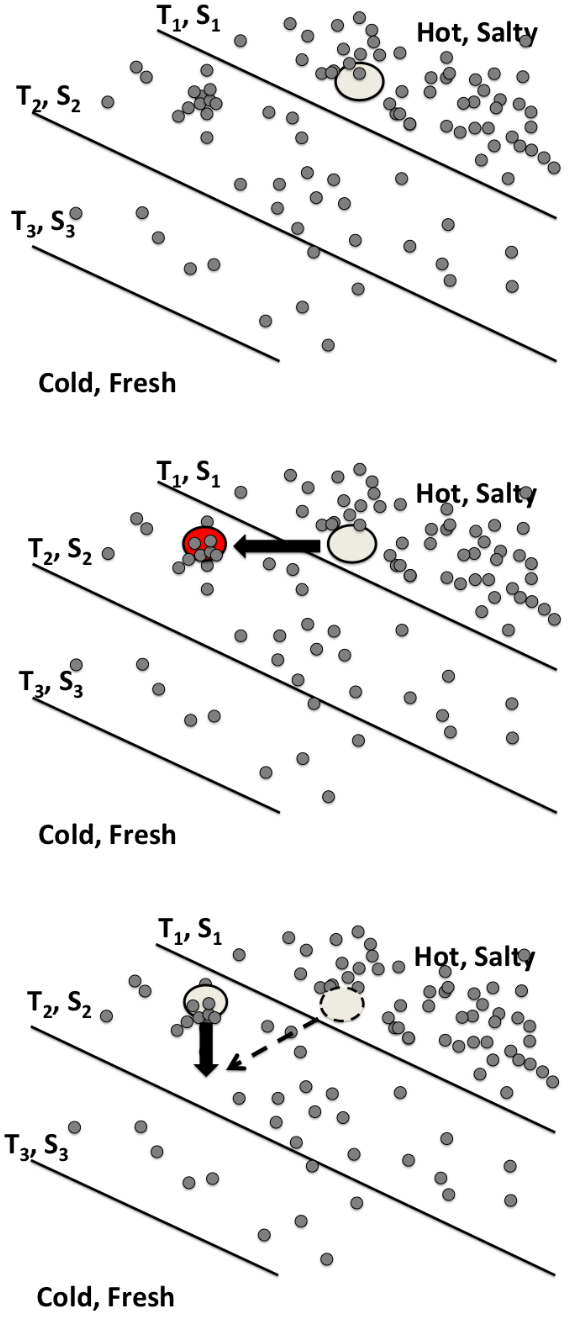

Figure 11: Fingering in the case of lateral intrusions. Here, $T_1 > T_2 > T_3$ and similarly $S_1 > S_2 > S_3$. The dark lines represent isotherms and isohalines.

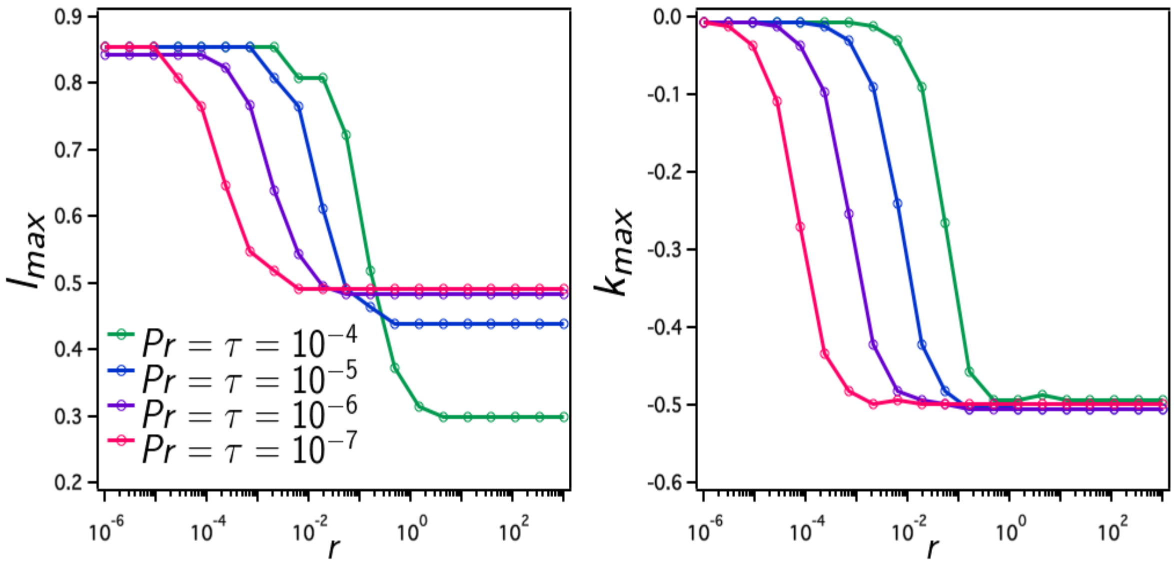

Figure 12: l_{max} and k_{max} vs r for the direct modes. We see that for $Pr = \tau \to 10^{-7}$, $l_{max} \to -k_{max}$.

It can be shown (see Appendices) that for $Pr \approx \tau \approx 10^{-6}$ and $\phi \approx 10^{-3}$ as $R_0 \to \infty$ that at stellar parameters, the direct mode have

$$\lambda_{max} \approx \sqrt{\frac{-klPr\phi}{|k|^2}} \qquad \text{for } k < 0 \tag{55}$$

Maximizing this result with respect to l or k results in the following constraint:

$$k_{max}^2 = l_{max}^2 \tag{56}$$

where, k_{max} and l_{max} are the vertical and horizontal wave numbers corresponding to the fastest growing mode λ_{max}. Since direct modes have $Im(\lambda) = 0$, we conclude

$$k_{max} = -l_{max} \tag{57}$$

We plot the approximated prediction for the direct growth rate (Equation (55)) as dark horizontal lines in Figure 10. As expected, they approximate λ_{max} for $Pr, \tau \ll 1$ reasonably well. We find that, to leading order, the angle with respect to the horizontal at which these fingers fall is $\theta \approx tan^{-1}(-1) = -45^{\circ}$. Finally, we plot the numerical values of l and k as a function of r for the direct modes in Figure 12. We notice that the result - that $k_{max} = -l_{max}$ as $R_0 \to \infty$ - is true in the case $Pr, \tau \to 10^{-7}$ and 10^{-6}; but begins to breakdown for $Pr \approx \tau > 10^{-5}$. The reason for this is that Equation (55) assumes $\phi \sim Pr^{\frac{1}{2}}$. Since $\phi = 10^{-3}$ in Figure 12, this approximation becomes invalid in the case $Pr \approx \tau > 10^{-6}$.

3.1.2 Oscillatory Modes

Figure 13 shows flower plots corresponding to Pr $= \tau = 10^{-6}$ at $R_0 = 1.2$ and 10^5, with $\phi = 10^{-3}$. We find, just as in the oceanic regime, that the fingering modes (i.e. modes with $Im(\lambda) = 0$) dominate over the oscillatory modes at both high and low R_0. According to the flower plots given in Figure 13, the oscillatory modes occur exclusively for $k > 0$. In addition, the vertical wave numbers of the fastest growing oscillatory modes are roughly the same order as those in the salty water regime. Notice that the oscillatory modes exist for very small positive values of k - implying that the length scale of the oscillatory modes are fairly large. We see typical values of k that correspond to oscillatory modes are $k_{max} \approx .005$. This corresponds to a wavelength of 1200d in the vertical. In the horizontal direction, the length scale of these modes is much larger since $l \approx 10^{-6}$ - which corresponds to $10^7 d$. Since $d \approx 10$ m, the wavelengths in the vertical and horizontal corresponding to $Pr \approx \tau \approx 10^{-6}$ are $\approx 10^4$ m and 10^8 m, respectively.

For perspective, the diameter of the Sun is about 10^9 m. The diameters of red giants range roughly $20 - 100$ the diameter of the sun. Now most of the interior of red giants - except for a small region surrounding the core where the μ inversion takes place - is fully convective. This suggests that the possibility that these modes may be present in a star is small. Still, if the these oscillatory modes do exist - their predicted length scales imply they are global phenomena - which is interesting since such large-scale modes are potentially observable.

We find that the $Re(\lambda_{max})$ changes little as R_0 varies, as seen in Figure 14. Moreover, we find that

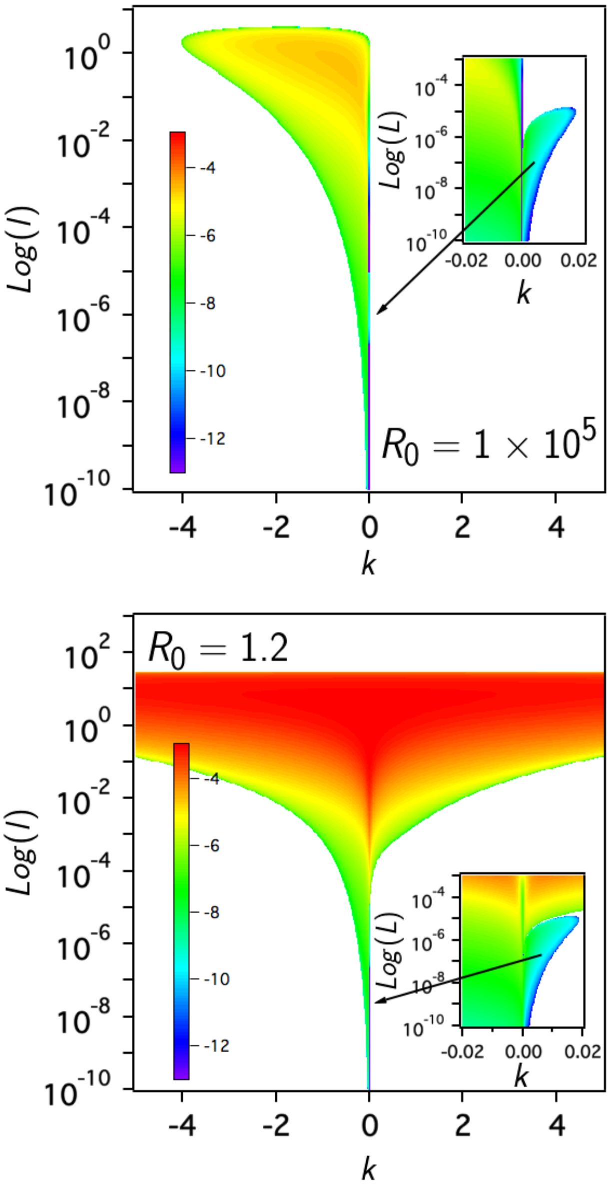

Figure 13: Flower Plots obtained by solving equation (51) for λ for Pr = τ= 10^{-6} and $\phi = 10^{-3}$. The oscillatory modes are given by the small k "leaf" structures.

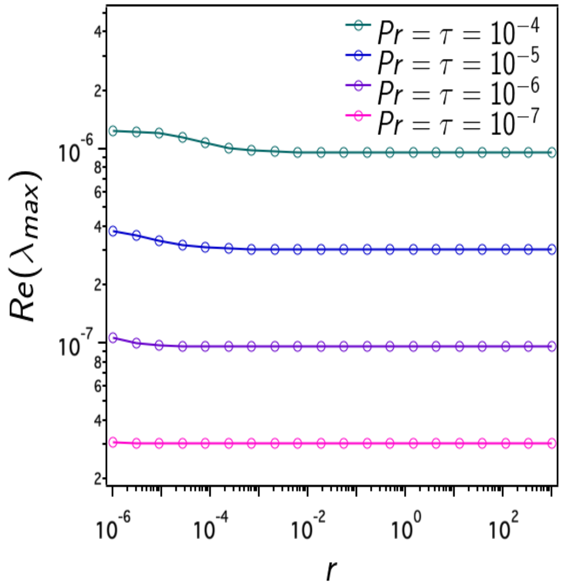

Figure 14: λ_{max} vs r for the oscillatory modes at $\phi = 10^{-3}$ for $Pr = \tau$ varying between 10^{-4} and 10^{-7}.

the wave numbers l_{max} and k_{max} exhibit the same behavior. It can be shown that in the oscillatory case (see Appendix), the wave numbers associated with the fastest growing mode are related by:

$$k_{max} \approx \frac{l_{max}}{\phi} \tag{58}$$

Indeed, we find that the vertical wavenumber k is roughly 3 orders of magnitude smaller than the horizontal wavenumber l. We also find numerically that $k_{max} \sim O(\phi)$, so $l_{max} \sim O(\phi^2)$.

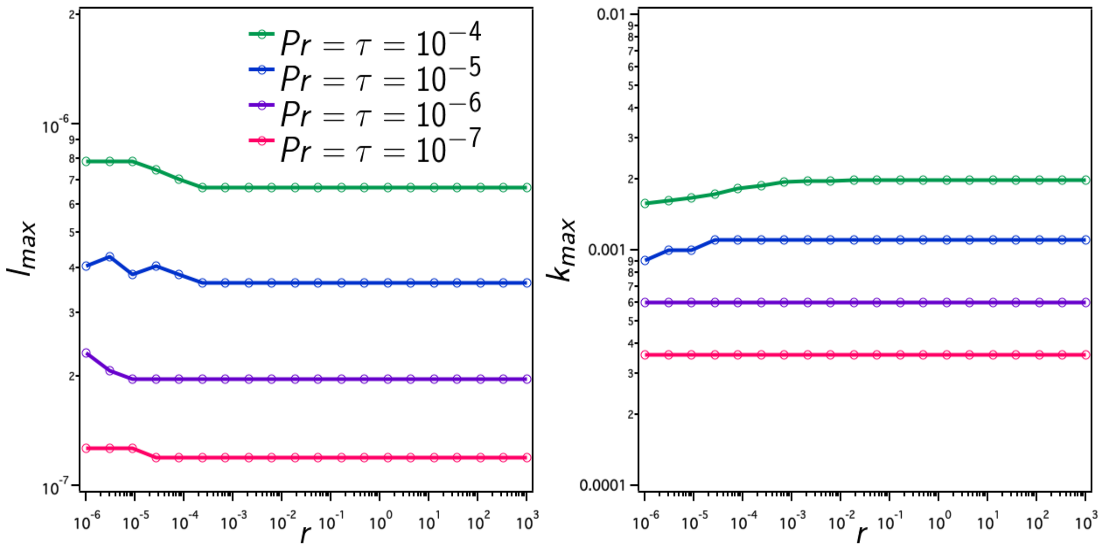

Figure 15: l_{max} and k_{max} vs r for the oscillatory modesfor $Pr = \tau$ varying between 10^{-4} and 10^{-7} and $phi = 10^{-3}$.

3.2 The Turbulent Case: The Collective Instability at $\phi = 0$

In this section, we now investigate the possibility of exciting the collective instability and begin with the case where $\phi = 0$, in which case we do not expect intrusions to be excited. Unlike the laminar case - which sets $A_1 = A_2 = 0$, $Nu_0 = 1$ - we now calculate these coefficients according to Equation (23) and (45) using the prescription described in Section 2. Since the basic fingering instability, which is responsible for the small scale turbulent fluxes required for the development of the collective instability, only exists for $1 < R_0 < 1/\tau$ i.e. $(r < 1)$, we now limit our analysis to that range. We plot the $Log(Re(\lambda))$ as a function of horizontal and vertical wave numbers l and k for $Pr, \tau = 10^{-6}$ at $R_0 = 10^5$ $(r \approx .1)$ and $R_0 = 1.2$ $(r \approx 10^{-7})$ in Figure 16. We provide the values of the coefficients calculated (see Section 4.2) in Table 1 below.

We plot the largest oscillatory growth rates as a function of non-dimensional r for Pr and τ in Figure 17a. We find that the collective instability can exist at relatively large values of Pr, τ (e.g. $Pr, \tau > 10^{-3}$), but for $Pr = \tau < 10^{-3}$, no oscillatory modes are found. In addition, we find that oscillatory modes only exist

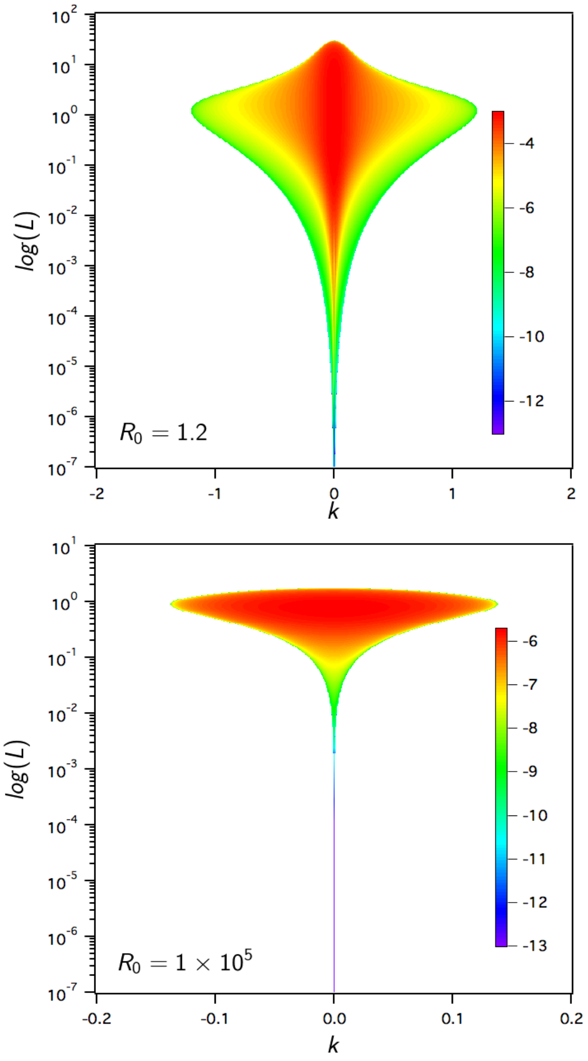

Figure 16: Flower Plots obtained by solving equation (51) for λ for Pr = τ= 10^{-6} and $\phi = 0$.

for smaller values of r, but disappear as r increases. The predicted range in r of the collective instability actually decreases as Pr and τ decrease.

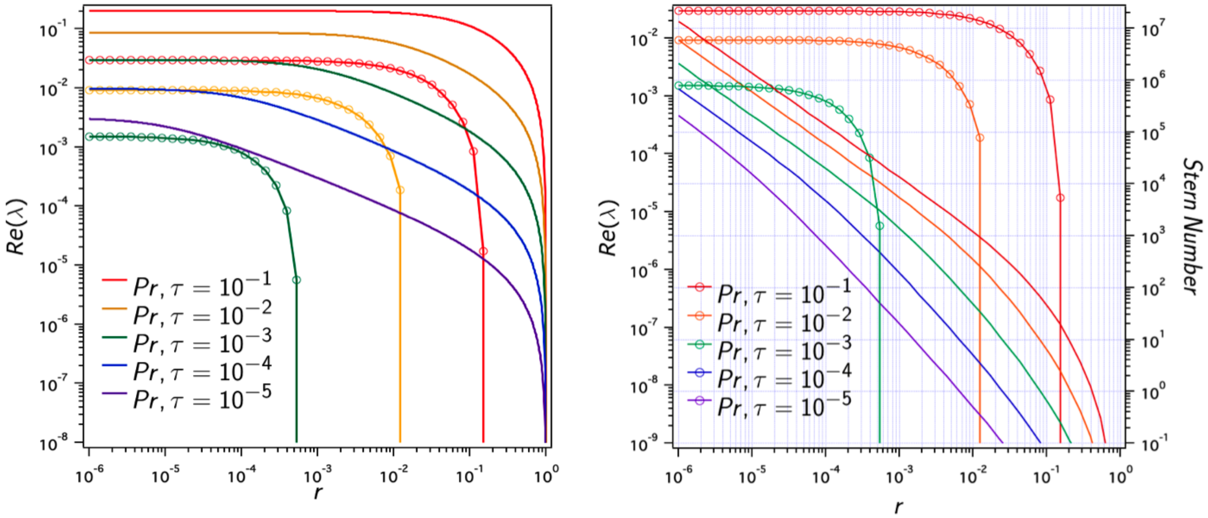

Figure 17: The Collective Instability and Fingering Instability growth rates for $\phi = 0$. Left: lines with circle markers represent oscillatory modes and solid lines represent the fingering mode. Right: lines with circle markers represent oscillatory modes and solid lines represent the stern number (see equation 59).

Table 1: Comparison of Coefficients for $Pr = \tau = 10^{-6}$, and $R_0 = 1.2$ ($r \approx 2 \times 10^{-7}$) and $R_0 = 10^5$ ($r \approx .1$)

	$r = .1$	$r = 2 \times 10^{-7}$
A_1	-1.11	-322.51
A_2	-6.52e-10	-8.16e-5
γ	.40	1.5e-3
Nu_T	1.00	1.00
Nu_S	111.25	63218.92

According to Stern et al. (2001), a system should be unstable to the collective instability if the Stern number, defined as

$$A = \frac{(Nu_T - 1)(\gamma_{turb}^{-1} - 1)}{Pr(1 - R_0^{-1})} \tag{59}$$

is greater than one.

Fig. 17b plots the observed oscillatory modes as a function of r on the left axis and the Stern Number on the right axis. We observe that oscillatory modes aren't excited at all for Pr and $\tau < 10^{-3}$ despite the fact that it is still possible for the constraint $A > 1$ to be satisfied even for $Pr, \tau = 10^{-6}$. This suggests that the Stern number may not adequately describe the transition from stability to instability for collective modes at low Pr. This is another example of a situation in which results obtained in the oceanographic context do not apply to the astrophysical one.

Our results are on the other hand consistent with the conclusion given in Denissenkov and Merryfield (2011) - that it is unlikely that the collective instability can explain the hidden mixing problem in RGB stars. However, while their calculation was based on rough estimates for the turbulent transport caused by basic fingering, our results are much more robust and reliable.

3.3 The Turbulent Case: Oscillatory and Intrusive Modes at $\phi = 10^{-3}$

We now investigate the solutions of Equation (51) in the case $\phi = 10^{-3}$. As in the previous section, the turbulent flux coefficients A_1, A_2, and Nu are calculated according to (23) and (45) and we limit our analysis to the range $0 < r < 1$. As in the previous sections, we produce flower plots for $Pr, \tau = 10^{-6}$ for $R_0 = 1.2$ and $R_0 = 10^5$ (Figure 18). A quick comparison of the flower plots generated here with those in the laminar regime in which $\phi \neq 0$ demonstrates that many parallels exist between the laminar and turbulent regimes.

3.3.1 Direct Modes:

Notice how as r grows, the unstable domain shrinks and retreats to a region where $k < 0$ - nevertheless leaving a broad spectrum in l where direct modes can be excited. We find that the latter are very similar to

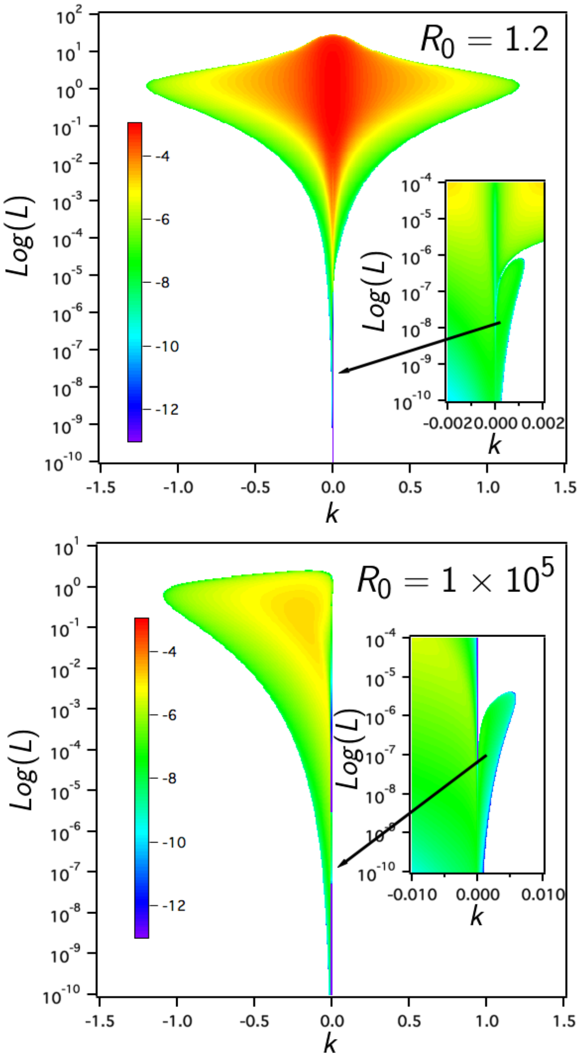

Figure 18: Flower Plots obtained by solving the Equation (51) for λ for $Pr = \tau = 10^{-6}$ and $\phi = 10^{-3}$. Both direct modes (main plot) and oscillatory modes (see inset) are presented.

the laminar intrusive modes discussed in Section 5.1.1. Moreover, the predictions for wave numbers l_{max} and k_{max} of the fastest- growing direct modes given in Equation (57), for large R_0 appear to be valid approximations in the turbulent regime as well, and have, in the case of the intrusive mode, $l_{max} \approx -k_{max} \approx 0.4$. We also plot λ_{max} as a function of r at various Pr, τ in Figure 19. Since $Nu_0 \to 1$ as $r \to 1$ (Brown et al., 2013), it is not surprising to see that the growth rates of the "turbulent" modes tend to approach the growth rates of the "laminar" modes (which are obtained when $Nu_0 = 1$).

In addition, we plot λ_{max} as a function of r at $Pr = \tau = 10^{-7}$ at various values of ϕ. We find that the effect of decreasing ϕ is to decrease λ_{max} as $r \to \infty$. We recover the behavior we might expect based upon the approximate solutions for λ_{max} in Section 5.1 (see Equation (56)).

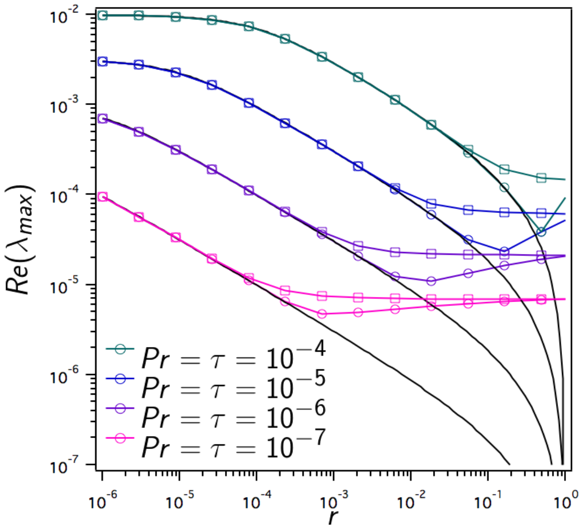

Figure 19: λ_{max} for direct modes as a function for r. The lines with circle markers represent turbulent direct modes. The lines with square markers represent laminar modes (i.e. $A_1 = A_2 = 0$ and $Nu = 1$). Solid lines represent the fingering mode when $\phi = 10^{-3}$.

3.3.2 Oscillatory Modes

We see from the flower plots in Figure 18, in the large R_0 case that, $k_{max} \approx .005$ and $l_{max} \approx 10^{-6}$ - a result we might expect in the case of a laminar fluid (recall Equation (59) from Section 5.1.2). We plot λ_{max}

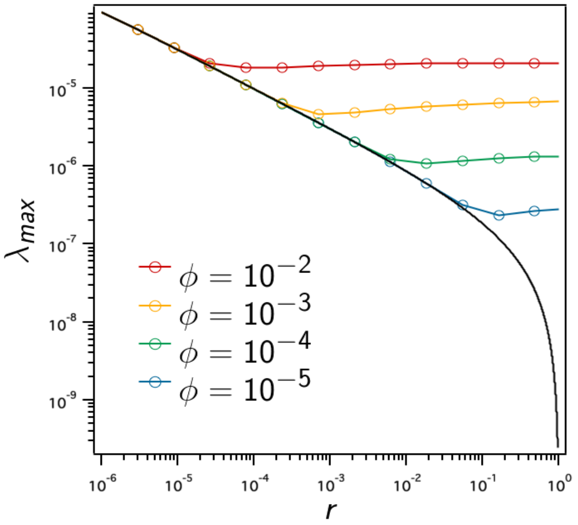

Figure 20: λ_{max} for direct modes as a function for r at Pr, $\tau = 10^{-7}$ at various ϕ. The solid dark line represents the fingering mode. Lines with markers represent the turbulent case.

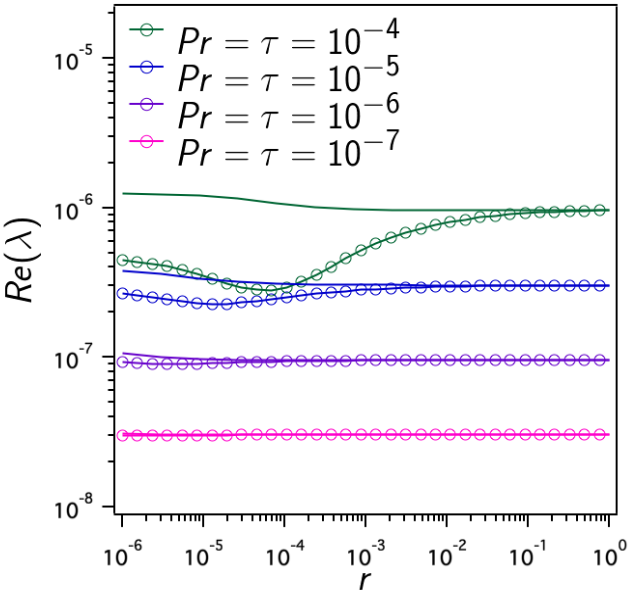

Figure 21: λ_{max} for oscillatory modes as a function for r at Pr, $\tau = 10^{-7}$ at $\phi = 10^{-3}$. The solid lines represent the numerical predictions corresponding to the laminar case. Lines with markers represent the numerical predictions corresponding to the turbulent case.

for the oscillatory modes as a function of r in Figure 21. We find λ_{max} is relatively constant in the astrophysical parameter regime (i.e. $Pr = \tau = 10^{-7}$) as R_0 is varied - just as in the laminar regime. Moreover, as $Pr, \tau \to 10^{-7}$, the growth rates of the laminar and "turbulent" modes also converge to one another. This is consistent with the results from the previous section- at such low Pr and τ the "turbulent" diffusivities are very small, and the system essentially behaves as if the background fingering flux was negligible.

There is one caveat in this analysis that needs to be pointed out. The basic fingering mode in the case $\phi = 0$ is described in Section 3.2 - 3.3 and Brown et al. (2013) and is used to calculate Nu_0, γ_0, A_1, and A_2 coefficients that enter into Equation (51). However, Brown et al. (2013)'s theory does not apply when $\phi \neq 0$. When $\phi \neq 0$, we must find some other estimate for Nu_T and Nu_μ that better model transport by the new inclined modes we discovered in Section 3.1.1. This problem is left for future studies.

4 Conclusion

The objective of this work was to see if any modes excited by double diffusive instabilities can explain the missing mixing in stellar interiors on the RGB. The motivation for looking at double diffusive instabilities (as opposed to studying instabilities due to rotation, magnetism, etc.) stems from the presence of an inverse molecular weight inversion generated in the external wing of the hydrogen burning shell after the first dredge up (See Section 1.1). The effect of the μ inversion is to create an unstable stratification for the slowly diffusing component of density. Moreover, since entropy, the quickly diffusing component, is stable, the interior of the star has stratifications that could drive the fingering instability. Therefore, it is possible that some of the hidden mixing on the RGB may be due to double diffusive processes of which are described by Equation (51) from Traxler et al. (2011).

In this work, we've undertaken a semi-analytic investigation of both laminar and mean-field double-diffusive instabilities, combining the works of Traxler et al. (2011) in the astrophysical regime with the recent results of Brown et al. (2013). We began with the laminar case ($A_1 = A_2 = 0$ and $Nu_0 = 1$) and obtained some approximations for the growth rates of fingering modes and other modes at low Prandtl number and diffusivity ratio.

We discovered that if a lateral gradient exists, fingers will continue to form even in systems that are nominally stable to basic fingering convection. The length scale and growth rate of these inclined fingers are roughly the same order of magnitude as those where there is no lateral gradient. For systems in which $Pr, \tau \approx 10^{-7}$, these fingers will fall at an angle 45° to the horizontal.

The oscillatory modes, on the other hand, are characterized by fairly large length scales and very small growth rates. In the case $Pr \approx \tau \approx 10^{-6}$, their wavelength along the horizontal is $\sim 10^8$ m -which is of the order of magnitude of the diameter of many stars. We acknowledge that the possibility that these modes exist is a bit dubious since the fingering region - that is, the region of the star that experiences an inverse μ gradient - definitely does not extend the entire span of the star.

In addition to laminar instabilities, we explored the possibility of mean-field or "turbulent instabilities". We found that the collective instability - which refers to the excitation of large scale oscillator modes - is not present for $Pr, \tau < 10^{-3}$. This means that the collective instability cannot explain the missing mixing along the RGB. In the case where there is a lateral gradient, we essentially recover the fastest growing mode of the laminar oscillatory and direct modes.

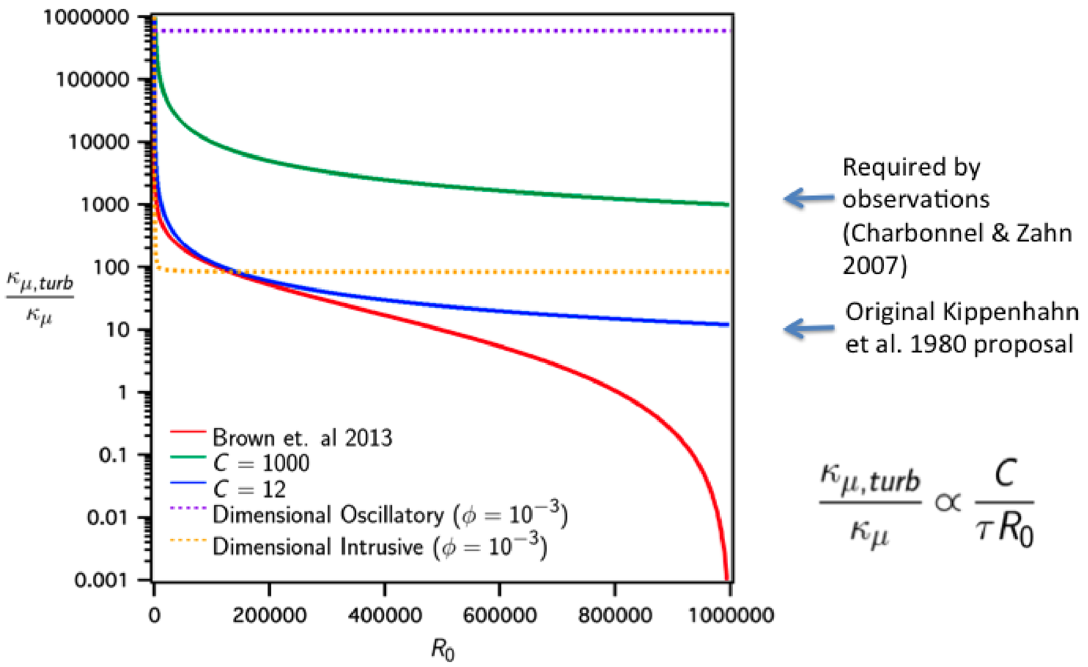

Figure 22: A comparison of the diffusion coefficients as a function of R_0.

We close this section by estimating the rate of compositional mixing for oscillatory and direct modes (See Section 3.3). The appropriate way to calculate an associated turbulent diffusivity would be to follow the procedure discussed in section 4.2 in Brown et al. (2013). However, for lack of time, we opt instead for a "rough" estimate based on dimensional analysis. Dimensional analysis of the diffusion coefficient implies that $D \propto \left[\text{length}\right]^2/\left[\text{time}\right]$. A good estimate for a typical length scale is the wavelength of the fastest growing mode and similarly, a good estimate for a typical timescale is the growth rate of the fastest growing mode. Hence, the diffusivity is:

$$\kappa_{\mu,\,\text{turb}} = \frac{\lambda_{max}}{k_{max}^2}\kappa_T$$

By definition, $\tau = \kappa_\mu/\kappa_T$. This implies:

$$\frac{\kappa_{\mu,\,turb}}{\kappa_\mu} \approx \frac{\lambda}{\tau k^2} \tag{60}$$

Note that we chose the vertical wavenumber to be the relevant parameter, since the fingers will tend to fall in the $-\hat{\mathbf{e}}_z$ direction. For the direct laminar instability discussed in Section 3.1.1, in the systems where, $Pr = \tau = 10^{-7}$ and $\phi = 10^{-3}$, $\lambda_{max} \approx 7 \times 10^{-7}$, $k_{max} = -.51$, and $l_{max} = .5$ as $R_0 \to \infty$. We calculate the diffusion constant to be: $D = \kappa_{\mu,\,turb} \approx 2.8 \times 10^2 \kappa_\mu$ as $R_0 \to \infty$. The value of D seems reasonable since it is quite similar to that calculated through dimensional analysis from Brown et al. (2013) at low R_0 (See Figure 19).

Finding the diffusion constant corresponding to the oscillatory modes is a little bit more complicated, since there are two typical timescales in the problem: the mode growth rate and the mode period. However, here we can draw from the work of Buhler et al. (2013). Buhler et al. (2013) completed an extensive study on estimating the diffusion constant for diffusive oscillatory waves. They find the turbulent diffusivity of oscillatory waves with frequency ω_0 and damping rate α_0:

$$D = E\left[u^2\right]\frac{\alpha_0}{\omega_0^2 + \alpha_0^2} \tag{61}$$

where $E\left[u^2\right]$ represents the kinetic energy of the system, α_0 is the damping, and ω_0 is the angular frequency of the oscillations. According to the linearized dimensional Boussinesq equations, $\alpha_0 = \kappa_T\left|k_{max}\right|^2$ where $\left|k_{max}\right|^2 = k_{max}^2 + l_{max}^2$ and $\omega_0 = Im(\lambda_{max})$. In addition, we assume $E = w^2$, where w is the vertical velocity field. Using dimensional analysis, we find $w \propto \lambda_{osc}/k = Im(\lambda)/k_{max}$. With these substitutions into (61), the equation for the diffusion constant corresponding to oscillatory motion becomes:

$$D = \frac{\lambda_I^2 \left|k\right|^2}{\tau k^2 \left(\lambda_I^2 + \left|k\right|^4\right)} \tag{62}$$

Based on Figure 22, we see that in the case where there exists a lateral gradient, the intrusive mode and oscillatory mode have the potential to explain the mechanism for the hidden mixing in low mass stars along the RGB. The predicted mixing rate for the intrusive mode suggest that its mixing plays a greater role, at large R_0, in regions of the inverse μ gradient that might otherwise be stable to the basic fingering instability. From Figure 22, we see that the oscillatory mode, owing to its fairly large length scale, has a mixing rate larger than what is required by observation.

The next step for this work is to verify that the modes described here actually exist via numerical simulations. Modeling the oscillatory modes will require a combination of fairly large length scales and small growth rates, which will likely require large computational times. Recall, from Section 3.1.2, we pointed out that for Pr, $\tau \approx 10^{-6}$, the length scale in the horizontal and vertical are $\sim 10^7 d$ and $\sim 10^4 d$, respectively. For perspective, a 'typical' simulation domain from Traxler et al. (2011) is $83.75d \times 83.75d \times 268d$. So to simulate these waves, the domain size of the simulation box should be at least $\sim 10^7 d$ and $\sim 10^4 d$ in the horizontal and vertical - which implies $\sim 10^5 d$ more mesh points. Another characteristic of the oscillatory modes is that they should be able to exist in 2D domains (as opposed to 3D). And so, to decrease computational time, the domain size of the simulation region might consist of very large dimensions in $\hat{\mathbf{e}}_x$ and $\hat{\mathbf{e}}_z$ and a small slice in $\hat{\mathbf{e}}_y$. The intrusions for $\phi \neq 0$, on other hand, should be much easier to observe since their length scales are $\sim 10d$.

Appendices

A The Method of Dominant Balances: Intrusions

We now seek to approximate the growth rate of the fastest growing intrusive mode by using the method of dominant balance. We make the following assumptions:

Assumption 1: $k,\ l = O(1)$

Assumption 2: $R_0 \to \infty\ \ \big(R_0 \gg 1/\tau\big)$

Assumption 3: Pr, τ are small, $Pr \approx \tau$

Let $\tau = \alpha Pr$ where $\alpha = O(1)$

Assumption 4: $1 \ll \phi \ll Pr\,, \tau$

In the case $Nu_0 = 1$ and $A_1 = A_2 = 0$, the coefficients of Equation (52) can be written as:

$$a_2 = \left|k\right|^2 + O(Pr) \tag{63}$$

$$a_1 = \left|k\right|^4 Pr(1+\alpha) + Pr\frac{l^2+m^2}{\left|k\right|^2} + O(Pr^2) \tag{64}$$

$$a_0 = \left|k\right|^6 \alpha Pr^2 + \alpha Pr^2(l^2+m^2) + kl\phi Pr \approx\ kl\phi Pr + O(Pr)^2 \tag{65}$$

In the last coefficient, by Assumption 4, we assume $Pr^2 \ll Pr\phi$. Substituting (63 - 65) into the Equation (52) gives:

$$\lambda^3 + \left|k\right|^2\lambda^2 + \left[\left|k\right|^4(1+\alpha) + \frac{l^2+m^2}{\left|k\right|^2}\right]Pr\lambda + klPr\phi = 0 \tag{66}$$

We use the method of dominant balance in order to determine the order of magnitude of each of the terms in Equation (52). The idea is to pick some number of terms to “balance” the left hand side. By balance we mean that the terms we pick are assumed to be much larger than the remaining terms in the polynomial and therefore, if the right hand side is equal to zero and all the other terms in the polynomial are neglected, the large order terms we pick should cancel to equal the right hand side.

For our problem, we assume solutions of the form:

$$\lambda = \lambda_0 Pr^{\beta} \text{ where } \lambda_0 = O(1) \tag{67}$$

In the case $A_1 = A_2 = 0$ and $Nu_0 = 1$ (i.e. the Laminar Case), Equation (66) becomes:

$$\lambda_0^3 Pr^{3\beta} + |k|^2 \lambda_0^2 Pr^{2\beta} + \left[|k|^4 (1+\alpha) + \frac{l^2 + m^2}{|k|^2} \right] Pr^{1+\beta} \lambda_0 + klPr\phi = 0 \tag{68}$$

Now, if $\beta > 0$, then $Pr^{2\beta} \gg Pr^{3\beta}$. We see immediately that for $\beta > 0$, the cubic term will always be negligible. And so, there exists only three possibilities that yield a balanced polynomial; only one of which is true. They are as follows:

$$Pr^{2\beta} \sim Pr^{1+\beta} \tag{69}$$

$$Pr^{1+\beta} \sim Pr\phi \tag{70}$$

$$Pr^{2\beta} \sim Pr\phi \tag{71}$$

Now, the first possibility, implies that $\beta = 1$. It follows that $Pr^{2\beta} \sim Pr^{1+\beta} \sim Pr^2$. By choosing this value for β, we assume that all other terms aside from those involving $Pr^{2\beta}$ and $Pr^{1+\beta}$ are negligible. This value for β cannot be the correct one, since according to Assumption 4, $Pr\phi \gg Pr^2$. We reject this value of β because it is inconsistent with Assumption 4.

What about option 2? Since, for the systems we're concerned with $\phi \sim Pr^{\frac{1}{2}}$, we re- write Option 2 as:

$$Pr^{1+\beta} \sim Pr^{\frac{3}{2}} \tag{72}$$

In this option, we seek to balance the $Pr^{1+\beta}$ term with $Pr\phi$. And so, we assume the possibility that $Pr^{2\beta}$ is negligible. For this option, the $\beta = 1/2$. From this, it follows $Pr^{1+\beta} \sim Pr\phi = Pr^{\frac{3}{2}}$. Now the term we neglected was $Pr^{2\beta} = Pr$ for $\beta = \frac{1}{2}$. This option, like the last one, results in an inconsistency since the term we neglected is larger than the terms we considered might balance Equation (68).

Possibility 3 assumes $Pr^{2\beta} \sim Pr\phi$. With the assumption that $\phi \sim Pr^{\frac{1}{2}}$ becomes:

$$Pr^{2\beta} \sim Pr^{\frac{3}{2}} \tag{73}$$

In this case, we assume that there is a balance between $Pr^{2\beta}$ and $Pr\phi$ and all the other terms are negligible. That is, if this is the correct option to obtain a dominant balance, $Pr^{2\beta} \sim Pr\phi \gg Pr^{1+\beta}$. For this balance, $\beta = \frac{3}{4}$. It follows that, $Pr^{\frac{3}{2}} \gg Pr^{\frac{7}{4}}$ - which unlike the other options is consistent. Substituting $\beta = \frac{3}{4}$ into Equation (68) and dropping all the negligible terms gives:

$$\left|k\right|^2 \lambda^2 + klPr\phi \approx 0 \tag{74}$$

Solving for λ gives:

$$\lambda \approx \sqrt{\frac{-klPr\phi}{\left|k\right|^2}} \tag{75}$$

where, k_{max} and l_{max} are the wave numbers corresponding to the fastest growing mode with growth rate λ_{max}. In order for the growth rate (75) to return a non-imaginary result (since intrusive/fingering modes have $Im(\lambda) = 0$), we conclude

$$k_{max} = -l_{max} \tag{76}$$

Substituting (76) into (75), we find that in the case Pr and τ are very small,

$$\lambda_{max} \approx \frac{1}{2}\sqrt{2Pr\phi} \tag{77}$$

In order to find $l_{max} = l_{max}(Pr, \tau)$ and $k_{max} = k_{max}(Pr, \tau)$ we could maximize (66) with respect to either of the wave numbers, and complete the same analysis dominant balances analysis. For lack of time, we leave this as a future pursuit. A less rigorous approach to this problem is given in the following section.

B Rough Approximation for Intrusive Modes

Prior to learning about the Method of Balances we approached the problem of approximating λ_{max} and its corresponding wave numbers l_{max} and k_{max} in the following way. We include the work here.

We now seek to approximate the growth rate of the fastest growing intrusive mode as $R_0 \to \infty$ (or $r \to \infty$). According to Figure 10 for $Pr = \tau = 10^{-7}$, $\lambda_{max} \approx 10^{-5}$. We can approximate our cubic by a quadratic in λ in the case that the cubic term in (52) $\lambda^3 \ll a_2\lambda^2$, $a_1\lambda$, and a_0. If this constraint is satisfied, our cubic expression for the growth rate can be approximated by:

$$a_2\lambda^2 + a_1\lambda + a_0 = 0 \text{ or } \lambda^2 + \frac{a_2}{a_1}\lambda + \frac{a_0}{a_1} = 0 \tag{78}$$

This is convenient since solutions of this polynomial are given by the quadratic formula:

$$\lambda = -\frac{a_1}{2a_2} \pm \frac{1}{2}\sqrt{\left(\frac{a_1}{a_2}\right)^2 - 4\frac{a_0}{a_2}}$$

Discarding the negative root (since such a solution would correspond to a negative growth rate) and substituting coefficients a_2, a_1, and a_0 gives:

$$\lambda = \frac{-Prl^2}{2|k|^4} + \frac{1}{2}\sqrt{\frac{Pr^2l^4}{|k|^8} - \frac{4\tau Prl^2}{|k|^2} - \frac{4Prlk\phi}{|k|^2}} \tag{79}$$

For the systems we are concerned with, $Pr, \tau \approx 10^{-7}$ and $\phi \approx 10^{-3}$. We discard the first and second terms in the radical and keep the last term since $Pr\tau \sim Pr^2 \ll Pr$. In addition, since we assume $Pr \ll \phi$, the product $\sqrt{Pr\phi} > O(Pr)$. For this reason, we discard the first term as well.

This implies that for small Pr, τ, the growth rate of the fastest growing intrusive mode to leading order is approximately:

$$\lambda \approx \frac{1}{2}\sqrt{-\frac{4Prlk\phi}{|k|^2}} \tag{80}$$

where, $\left|k\right|^2 = k^2 + l^2$. Maximizing (80) with respect to either k or l results in the following constraint:

$$k_{max}^2 = l_{max}^2$$

where, k_{max} and l_{max} are the wave numbers corresponding to the fastest growing mode with growth rate λ_{max}. In order for the growth rate (80) to return a non-imaginary result (since intrusive/fingering modes have $Im(\lambda) = 0$), we conclude

$$k_{max} = -l_{max} \tag{81}$$

Substituting (81) into (80), we find that in the case Pr and τ are very small,

$$\lambda_{max} \approx \frac{1}{2}\sqrt{2Pr\phi} \tag{82}$$

To solve for l, we maximize the quadratic (78) with respect to k. The derivative of Equation (78) with respect to k is given by:

$$b_2\lambda^2 + b_1\lambda + b_0 = 0 \tag{83}$$

where,

$$b_2 = 2k(1 + Pr + \tau) \tag{84}$$

$$b_1 = 4k(k^2 + l^2)(Pr + \tau + \tau Pr) - \frac{2kl^2 Pr}{(k^2 + l^2)^2} \tag{85}$$

$$b_0 = 6k(k^2 + l^2)^2 Pr\tau - lPr(\tau - 1)\phi \tag{86}$$

Again, we approximate the coefficients of this polynomial by assuming that Pr, $\tau \ll 1$. We discard all but the leading order terms in the in the coefficients b_2, b_1, and b_0. Then, the coefficients can be approximated as:

$$b_2 \approx 2k \tag{87}$$

$$b_1 \approx 4k(k^2 + l^2)(Pr + \tau) - \frac{2kl^2 Pr}{(k^2 + l^2)^2} \tag{88}$$

$$b_0 \approx lPr\phi \tag{89}$$

Substituting λ_{max} (see Equation (82)) and letting $l = -k$ into (83) with these approximated coefficients gives:

$$\frac{-1}{2}\frac{Pr}{k_{max}} + 8k_{max}^3(\tau + Pr) = 0$$

Solving for k_{max} in this expression gives:

$$k_{max}^4 \approx \frac{1}{16}\left(\frac{Pr}{\tau + Pr}\right) \tag{90}$$

So, in the case Pr, τ are very small and all but the leading order terms in in the coefficients in Equations (83 - 85) are negligible, the fastest growing direct mode have wave numbers and growth rate:

$$k_{max} \approx -\frac{1}{2}\left(\frac{Pr}{\tau + Pr}\right)^{1/4} \tag{91}$$

$$l_{max} \approx \frac{1}{2}\left(\frac{Pr}{\tau + Pr}\right)^{1/4} \tag{92}$$

$$\lambda_{max} \approx \frac{1}{2}\sqrt{2Pr\phi} \tag{93}$$

C The Method of Dominant Balances: Oscillatory Modes

We substitute $\lambda = \lambda_R + i\lambda_I$ into the original cubic (Equation (52)). Collecting imaginary terms gives:

$$\lambda_I^2 = 3\lambda_R^2 + 2a_2\lambda_R + a_1 \tag{94}$$

Doing the same for the real terms gives:

$$\lambda_I^2 - 3\lambda_R\lambda_I^2 + a_2\lambda_R^2 - a_2\lambda_I^2 + a_1\lambda_R + a_0 = 0 \tag{95}$$

Combining (94) and (95) results in the following cubic for λ_R:

$$\lambda_R^3 + b_2\lambda_R^2 + b_1\lambda_R + b_0 = 0 \tag{96}$$

where,

$$b_2 = a_2 \tag{97}$$

$$b_1 = \frac{1}{4}\left(a_2^2 + a_1\right) \tag{98}$$

$$b_0 = \frac{1}{8}\left(a_1a_2 - a_0\right) \tag{99}$$

We begin by making the same assumptions as in Appendix A. In addition, if we again write:

$$Pr = \alpha\tau \tag{100}$$

It follows that the coefficients of Equation (96) can be written as:

$$b_2 = |k|^2 + O(Pr) \tag{101}$$

$$b_1 = \frac{1}{4}\left(|k|^4 + |k|^4 Pr(1+\alpha) + Pr\frac{l^2+m^2}{|k|^2}\right) \approx \frac{1}{4}|k|^4 + O(Pr) \tag{102}$$

$$b_0 = \frac{1}{8}\left[\left(|k|^4 Pr(1+\alpha) + Pr\frac{l^2+m^2}{|k|^2}\right)|k|^2 - kl\phi Pr\right] \approx \frac{1}{8}\left[Pr|k|^2\left(|k|^4(1+\alpha) + \frac{l^2+m^2}{|k|^2}\right)\right] \tag{103}$$

Notice that for these coefficients, b_2, b_1, and $b_0 > 0$. This implies that the solutions of Equation (96) with coefficients (101 - 103) have negative roots or growth rates but no positive ones. And so we see, that the approximations made in Appendix A are invalid in the oscillatory case.

D Rough Approximation for Oscillatory Modes

Again, we attempt to find an analytic approximation to λ_{max} for oscillatory modes in order to understand this behavior. We seek to approximate these coefficients such that Pr, $\tau \ll 1$. Unfortunately, we see from Figure 13 that $k_{max} \not\approx l_{max}$ and therefore Equation (79) is not valid here. According to Fig 13, the wave numbers for oscillatory modes are related to each other roughly by $k \sim l^{\frac{1}{2}} \sim Pr^{\frac{1}{2}}$. The coefficients of the original cubic can be approximated by:

$$a_2 = \left|k\right|^2\left(1 + Pr + \tau\right) \approx k^2 \tag{104}$$

$$a_1 = \left|k\right|^4\left(\tau + Pr + \tau Pr\right) + \frac{Prl^2}{\left|k\right|^2}\left(1 - \frac{1}{R_0}\right) \approx \frac{Prl^2}{k^2}\left(1 - \frac{1}{R_0}\right) \tag{105}$$

$$a_0 = \left|k\right|^6\tau Pr + Prl^2\left(\tau - \frac{1}{R_0}\right) - Prlk\phi\left(\tau - 1\right) \approx Prl^2\left(\tau - \frac{1}{R_0}\right) + Prlk\phi \tag{106}$$

We substitute $\lambda = \lambda_R + i\lambda_I$ into the original cubic equation. Collecting imaginary terms gives:

$$\lambda_I^2 = 3\lambda_R^2 + 2a_2\lambda_R + a_1 \tag{107}$$

Doing the same for the real terms gives:

$$\lambda_I^2 - 3\lambda_R\lambda_I^2 + a_2\lambda_R^2 - a_2\lambda_I^2 + a_1\lambda_R + a_0 = 0 \tag{108}$$

Combining (107) and (108) results in the following cubic for λ_R:

$$\lambda_R^3 + b_2\lambda_R^2 + b_1\lambda_R + b_0 = 0 \tag{109}$$

where,

$$b_2 = a_2 \approx k^2 \tag{110}$$

$$b_1 = \frac{1}{4}\left(a_2^2 + a_1\right) \approx \frac{1}{4}k^4 \tag{111}$$

$$b_0 = \frac{1}{8}\left(a_1 a_2 - a_0\right) \approx \frac{1}{8}\left(Pr\,l^2 - Prlk\phi\right) \tag{112}$$

Notice that the density ratio appears nowhere in these coefficients. This implies that for these coefficients, the roots of the cubic (109) are also independent of R_0. We conclude that the terms involving R_0 in the unapproximated cubic (109) are minuscule. Unfortunately, a quick numerical analysis shows that $\lambda^3 \not\ll a_2\lambda^2$, $a_1\lambda$, and a_0. This means that the cubic (109) cannot be approximated by a quadratic. Instead, we use Cardano's method to represent the real root of Equation (109) since λ_R represents only the real part of λ. We define the following quantities according to Cardano's method:

$$Q \equiv \frac{1}{9}\left(3b_1 - b_2^2\right) \tag{113}$$

$$R \equiv \frac{1}{54}\left(9b_2 b_1 - 27b_0 - 2b_2^3\right) \tag{114}$$

$$D \equiv Q^3 + R^2 \tag{115}$$

$$S = \left(R + \sqrt{D}\right)^{1/3} \tag{116}$$

$$T = \left(R - \sqrt{D}\right)^{1/3} \tag{117}$$

So that,

$$\lambda_R = -\frac{1}{3}b_2 + S + T \tag{118}$$

Maximizing this result with respect to l gives the constraint:

$$l_{max} = \frac{k_{max}\phi}{2} \tag{119}$$

Alternatively, this wavenumber constraint could have been obtained by maximizing (109) with respect to l

instead. Substituting back into λ_R :

$$\lambda_R = \frac{1}{12}\Big(-4k^2 + \big(8k^6 + 27k^2 Pr\phi^2 - 3\sqrt{3}\sqrt{k^4 Pr\phi^2(16k^4 + 27Pr\phi^2)}\big)^{1/3} + \big(8k^6 + 27k^2 Pr\phi^2 + 3\sqrt{3}\sqrt{k^4 Pr\phi^2(16k^4 + 27Pr\phi^2)}\big)^{1/3}\Big) \tag{120}$$

Maximizing (120) with respect to k gives the result:

$$k_{max} \approx \left(\frac{9Pr\phi^2}{16}\right)^{1/4} \tag{121}$$

$$\begin{aligned}\lambda_{max} \approx{}& -0.25\left(Pr\phi^2\right)^{1/2} \\ &+ \left(0.014\left(Pr\phi^2\right)^{3/2} - \sqrt{0.00014Pr^3\phi^6 + 0.000046\left(Pr\phi^2\right)^3}\right)^{1/3} \\ &+ \left(0.014\left(Pr\phi^2\right)^{3/2} + \sqrt{0.00014Pr^3\phi^6 + 0.000046\left(Pr\phi^2\right)^3}\right)^{1/3}\end{aligned} \tag{122}$$

Although the result for λ_{max} in this case is not especially enlightening, we do learn about the properties of the wavenumber - namely why l_{max} is about three orders of magnitude less than k_{max}. These predictions for l_{max} and k_{max} imply very large length scales for the oscillatory modes. In addition, (119) and (122) recover a property we definitely expect; as $\phi \to 0$, the growth rate of the fastest growing mode in the oscillatory case goes to zero.

References

PG Baines and AE Gill. On thermohaline convection with linear gradients. *J. Fluid Mech.*, 37, 1969.

J. M. Brown, P. Garaud, and S. Stellmach. Chemical Transport and Spontaneous Layer Formation in Fingering Convection in Astrophysics. *ApJ*, 768:34, May 2013.

O. Buhler, N. Grisouard, and M. Holmes-Cerfon. Strong particle dispersion by weakly dissipative random internal waves. In *EGU General Assembly Conference Abstracts*, volume 15 of *EGU General Assembly Conference Abstracts*, page 1839, April 2013.

C. Charbonnel. Clues for non-standard mixing on the red giant branch from C-12/C-13 and C-12/N-14 ratios in evolved stars. A&A, 282:811–820, February 1994.

C. Charbonnel and J.P. Zahn. Thermohaline mixing: a physical mechanism governing the photospheric composition of low-mass giants. *Astron. Astrophys.*, 467(1), 2007.

D. S. P. Dearborn, J. C. Lattanzio, and P. P. Eggleton. Three-dimensional Numerical Experimentation on the Core Helium Flash of Low-Mass Red Giants. ApJ, 639:405–415, March 2006. doi: 10.1086/499263.

DSP Dearborn, DL Lambert, and J Tomkin. The c-12/c-13 ratio in stellar atmospheres. v-twelve k giants and subgiants. *The Astrophysical Journal*, 200:675–681, 1975.

P. A. Denissenkov and W. J. Merryfield. Thermohaline Mixing: Does it Really Govern the Atmospheric Chemical Composition of Low-mass Red Giants? ApJ, 727:L8, January 2011. doi: 10.1088/2041-8205/727/1/L8.

P. P. Eggleton, D. S. P. Dearborn, and J. C. Lattanzio. Deep Mixing of ^{3}He: Reconciling Big Bang and Stellar Nucleosynthesis. *Science*, 314:1580–, December 2006. doi: 10.1126/science.1133065.

P. P. Eggleton, D. S. P. Dearborn, and J. C. Lattanzio. The destruction of He by Rayleigh-Taylor instability on the first giant branch. In F. Kupka, I. Roxburgh, and K. L. Chan, editors, *IAU Symposium*, volume 239 of *IAU Symposium*, pages 286–293, May 2007. doi: 10.1017/S1743921307000567.

P. Garaud. Double-diffusive convection. *EAS Publications Series*, 63:285–295, 1 2013. ISSN 1638-1963. doi: 10.1051/eas/1363032. URL http://www.eas-journal.org/article_S1633476063000326.

K.K. Gilroy. Carbon isotope ratios and lithium abundances in open cluster giants. ApJ, 347:835–848, December 1989. doi: 10.1086/168173.

RG Gratton, C Sneden, E Carretta, and A Bragaglia. Mixing along the red giant branch in metal-poor field stars. *Astronomy and Astrophysics*, 354:169–187, 2000.

Rudolf Kippenhahn, Alfred Weigert, and Achim Weiss. *Stellar structure and evolution*, volume 282. Springer, 1990.

J. Lattanzio, D. Dearborn, P. Eggleton, and D. Dossa. Three Dimensional Simulations of the Core Helium Flash - with Rotation. *ArXiv Astrophysics e-prints*, December 2006.

A. Palacios and A. S. Brun. Simulation of turbulent convection in a slowly rotating red giant star. *Astronomische Nachrichten*, 328:1114, December 2007. doi: 10.1002/asna.200710857.

A. Palacios, C. Charbonnel, S. Talon, and L. Siess. Rotational mixing in low-mass stars. II. Self-consistent models of Pop II RGB stars. A&A, 453:261–278, July 2006. doi: 10.1051/0004-6361:20053065.

William H Press, Brian P Flannery, Saul A Teukolsky, and William T Vetterling. Numerical recipes in c: the art of scientific programming. *Section*, 10:408–412, 1992.

Timour Radko. *Double-diffusive Convection*. Cambridge University Press, 2013.

E. A. Spiegel and G. Veronis. On the Boussinesq Approximation for a Compressible Fluid. ApJ, 131:442–+, March 1960. doi: 10.1086/146849.

ME Stern, T. Radko, and J. Simeonov. Salt fingers in an unbounded thermocline. *J. Mar. Res.*, 59(3): 355–390, 2001.

A. V. Sweigart and J. G. Mengel. Meridional circulation and CNO anomalies in red giant stars. ApJ, 229: 624–641, April 1979. doi: 10.1086/156996.

A. Traxler, S. Stellmach, P. Garaud, T. Radko, and N. Brummell. Dynamics of fingering convection. Part 1 Small-scale fluxes and large-scale instabilities. *Journal of Fluid Mechanics*, 677:530–553, June 2011. doi: 10.1017/jfm.2011.98.

R. K. Ulrich. Thermohaline Convection in Stellar Interiors. ApJ, 172:165–+, February 1972. doi: 10.1086/151336.

David Walsh and Barry Ruddick. Double-diffusive interleaving in the presence of turbulence: The effect of a nonconstant flux ratio. *Journal of Physical Oceanography*, 30(9):2231–2245, 2000. doi: 10.1175/1520-0485(2000)030<2231:DDIITP>2.0.CO;2. URL http://journals.ametsoc.org/doi/abs/10.1175/1520-0485%282000%29030%3C2231%3ADDIITP%3E2.0.CO%3B2.

G. J. Wasserburg, A. I. Boothroyd, and I.-J. Sackmann. Deep Circulation in Red Giant Stars: A Solution to the Carbon and Oxygen Isotope Puzzles? ApJ, 447:L37, July 1995. doi: 10.1086/309555.